

# Comparative Study of Recurrent Neural Networks for Virtual Analog Audio Effects Modeling

Riccardo Simionato<sup>1\*</sup> and Stefano Fasciani<sup>1</sup>

<sup>1\*</sup>Department of Musicology, University of Oslo, Problemveien 11, Oslo,  
0313, Norway.

\*Corresponding author(s). E-mail(s): [riccardo.simionato@imv.uio.no](mailto:riccardo.simionato@imv.uio.no);  
Contributing authors: [stefano.fasciani@imv.uio.no](mailto:stefano.fasciani@imv.uio.no);

## Abstract

Analog electronic circuits are at the core of an important category of musical devices, which includes a broad range of sound synthesizers and audio effects. The nonlinear features of their passive and active electronic components give analog musical devices a distinctive timbre and sound quality, making them highly desirable. The development of software that simulates analog musical devices, known as virtual analog modeling, is a significant sub-field in audio signal processing. Artificial neural networks are a promising technique for virtual analog modeling. They have rapidly gained popularity for the emulation of analog audio effects circuits, particularly recurrent networks. While neural approaches have been successful in accurately modeling distortion circuits, they require architectural improvements that account for parameter conditioning and low-latency response. Although hybrid solutions can offer advantages, black-box approaches can still be advantageous in some contexts. In this article, we explore the application of recent machine learning advancements for virtual analog modeling. In particular, we compare State-Space models and Linear Recurrent Units against the more common Long Short-Term Memory networks. These have shown promising ability in sequence-to-sequence modeling tasks, showing a notable improvement in signal history encoding. Our comparative study uses these black-box neural modeling techniques with a variety of audio effects. We evaluate the performance and limitations of these models using multiple metrics, providing insights for future research and development. Our metrics aim to assess the models' ability to accurately replicate energy envelopes and frequency contents, with a particular focus on transients in the audio signal. To incorporate control parameters into the models, we employ the Feature-wise Linear Modulation method. Long Short-Term Memory networks exhibit better accuracy in emulating distortions and equalizers, while the State-Space model, followed by Long Short-Term Memory networks

when integrated in an encoder-decoder structure, outperforms others in emulating saturation and compression. When considering long time-variant characteristics, the State-Space model demonstrates the greatest capability to track history. The Long Short-Term Memory and Linear Recurrent Unit networks present more tendency to introduce audio artifacts, in particular, the Linear Recurrent Unit, which resulted in the least appropriate modeling techniques.

**Keywords:** Nonlinear Modeling, Virtual Analog, Audio Effect, Machine Learning

## 1 Introduction

The emulation of analog musical devices has become incredibly pervasive in digital commercial products. The distinct sound characteristics of both contemporary and old analog audio devices have captivated producers and musicians. Analog effect exists as standalone units as well as integrated with sound synthesizers. There are different types of popular effects such as filters, distortion, overdrive, compressor/limiter, as well as delay-based effects like chorus, flanger, phaser, and reverb. Analog circuits found in audio effects depend on intricately designed circuits that combine discrete passive and active electronic components to generate and modify electrical signals. Key components, such as operational amplifiers and diodes, are utilized in a variety of analog effects. These components present nonlinear behaviors that contribute to the unique sound of these devices. Accurate modeling of such nonlinearities is essential to replicate the behavior of analog audio devices. Consequently, the development of digital audio effects capable of simulating analog counterparts has become a crucial and valuable area of study within digital audio signal processing, often referred to as Virtual Analog (VA) modeling.

This article presents a comparative study that applies recent advancements in machine learning to audio effects modeling. Machine learning has become widely used in audio modeling and is often integrated into more traditional digital-signal-processing frameworks. Although hybrid solutions (referred to as gray-box approaches) have also been proposed, which offer their advantages [1], black-box approaches can still be appealing in some contexts. Gray-box approaches can incorporate physics knowledge [2] or measurements from systems [3]. While the former may not always be accurate enough, the latter may not be feasible for certain tasks. Universal black-box models have already been proposed [4], but these usually involve large networks that are not suitable for low-latency and real-time applications. In addition, while machine learning modeling of nearly all types of analog effects has been investigated, they often do not provide a satisfactory response when continuously manipulating conditioning parameters, needed to offer users runtime control over the effect's parameters.

In this study, we compare different recurrent artificial neural network architectures for modeling a selection of audio effects. In particular, we considered overdrive, saturator, low-pass filter, equalizer, and compressor. We selected audio effects with different complexities and time dependencies to investigate how these different architectural characteristics influence the results when learning directly from raw audio.

For black-box modeling purposes, Recurrent Neural Networks (RNNs) are often preferred among the different types of artificial neural networks. RNNs utilize internal states, which function as memory, making them particularly suitable in scenarios where time dependencies are crucial. Especially, when the inputs are limited to a small segment of digital audio samples, and the network does not have a large amount of input information to infer, as can happen with feed-forward architectures. Analog audio effects are dynamic physical systems that exhibit time-dependent characteristics: their output depends on previous internal states. Therefore, dynamic physical systems possess internal states that describe their physical evolution. This similarity to stateful machine learning architectures is often appreciated, as it allows for effective modeling of these systems.

The primary objective of this comparative study is to explore the capabilities of recurrent architectures in learning from raw digital audio and effectively modeling audio effects with different complexities. We aim to determine whether these architectures can learn various types of audio processing and be conditioned by control parameters found in audio effects. Additionally, we investigate whether novel machine learning architectures, which have shown remarkable results in sequence modeling, also perform well in the field of VA.

To address these questions, we apply models based on three different recurrent networks to a variety of audio effects: the popular Long Short-Term Memory (LSTM) [5], the State-Space models (SSMs) [6], and the Linear Recurrent Unit (LRU) [7]. All models consider conditioning on control parameters using the Feature-wise Linear Modulation (FiLM) method [8] and employ the Gated Linear Unit (GLU) [9]. For a fair comparison, we ensure that different models have similar numbers of layers and trainable parameters, as well as utilize the same amount of input audio samples.

Moreover, we design these architectures with a limited computational complexity, measured in the number of floating points operations per output audio sample, which is 1.500 FLOPs per sample or 72 MFLOPs per second at 48 KHz, ensuring theoretical real-time computational capabilities on consumer-grade devices. The designed architectures also present limited input-output audio latency, which we have limited to a maximum of 1.33 ms.

In this study, we do not consider Convolutional Neural Networks (CNNs) [10] although their integration with RNNs has the potential to enhance accuracy [11]. However, when working with small input vectors and considering long-term dependencies, an RNN-based structure with the ability to encode the signal’s history using the states is a particularly appealing feature. Therefore, in this study, our focus is solely on recurrent layers, and we do not include layers of different types from recurrent and fully connected layers.

Section 2 reviews the recent advancements in modeling analog devices, with a specific focus on the benefits and drawbacks of the recent deep learning methods against other data-driven methods. Section 3 details the methodology, architectures, losses, and datasets used in our experiments. Section 4 presents the obtained results and the consequent discussion on the limit and strength of the current methodology.

## 2 Background

There are two possible approaches for approximating a continuous-time system with a discrete-time model: physics-based and data-driven. Physics-based approaches discretize existing continuous-time models. Data-driven approaches identify a discrete model directly from discrete measurement data.

Physics-based modeling is used when comprehensive knowledge about the system is available. In the case of analog audio effects, this requires knowing the schematics of the circuits, and specific electronic components populating the system. In addition, the circuit and components need to be mathematically modeled and solvable. A numerical scheme has to be formulated and the obtained discrete equations have to be solved iteratively to produce the digital output sound. In the case of an implicit ordinary differential equations system, the Newton-Raphson (NR) iterative method is generally utilized to find the solutions. NR converges quadratically although this is not always guaranteed. As a consequence, physics-based models generally present a high computational cost.

Data-driven modeling is used when information on the inner circuitry of the audio effect is not available. The model is considered as a mapping between input-output data: input-output measurements are taken as a reference to find a suitable mapping that approximates the system response. There are three main components in the procedure leading to a data-driven model: the dataset, the set of candidate modeling techniques, and the validation procedure. The selection of input signals for which output is measured, the configuration of the effect's control parameters, and the data collection process have a major impact on the quality of the resulting model. Data-driven approaches rely on measurements that are static representations of the system behavior, leading to higher difficulty in accurately emulating its dynamical aspects.

Common examples of data-driven approaches are the block-oriented Hammerstein model, the Wiener model, and their combinations [12]. In the Wiener model, a linear model is followed by a static nonlinearity, while in the Hammerstein model is the opposite. These models have a convenient representation, and they are created by estimating the model coefficients from real data and with some error minimization techniques. A proposed method to classify whether the nonlinear system should rather be modeled by a Wiener or a Hammerstein model is in [13]. These approaches, for the reason of simplification, model linear and nonlinear behavior separately. Using this strategy two block types can be identified, linear dynamic blocks, and static nonlinearities.

Another data-driven approach for modeling analog circuits involves utilizing artificial neural networks (ANNs) [14]. ANNs are composed of interconnected units, where each connection can transmit a signal to other artificial neurons. These neurons receive and process signals, and they can transmit the signals to connected neurons. The signal transmitted through a connection is represented by a real number, and the output of each neuron is determined by a nonlinear function applied to the sum of its weighted inputs. Neural networks are trained by optimizing the network's parameters to minimize the error between the predicted output and the actual target values within a given dataset. Gradient-based techniques, such as backpropagation, are commonly employed to estimate the network's weights. Also in this scenario, it can be beneficial

to incorporate a specific block that focuses on the "unknown" behavior, while separately utilizing a different block to handle the "known" aspects that have already been accurately modeled.

## 2.1 Virtual Analog Modeling

Among physics modeling for analog effects, a popular method is based on the wave-digital principle [15]. Wave digital filters (WDF) are constructed by interconnecting simple discrete-time models of individual electronic components (inductors, capacitors, and resistors). Wave digital filters are digital filters based on physical modeling principles. Wave digital (WD) techniques were extensively investigated [16, 17]. Starting with linear elements, WD was expanded to handle nonlinear elements in [18]. More recent advances allowed the realization of multidimensional simulations with multiple nonlinearities [19]. In [20], authors showed how its quadratic convergence strongly depends on the free parameters and proposed a novel formulation using WD formalism. Recent VA works using this approach include vacuum tube based-circuits as the preamplifier circuit of an amplifier [21], cascaded amplifiers [22], envelope filter guitar effect [23], booster guitar pedal [24], and a ring modulator [25].

Other approaches consider directly deriving the finite-difference time-domain (FDTD) scheme from the continuous physical differential equations. In [26], this method is used to model an analog tape machine, while in [27], authors simulate the sonic effect of the Hammond tonewheel organ.

Port-Hamiltonian approach [28] uses the state-space description of power exchange between energy-storing parts, dissipative parts, and external sources in a circuit. Port Hamiltonian formalism has the advantage of preserving the power balance, a beneficial aspect in nonlinear cases [29]. A port-Hamiltonian formulation is found in [30], in which a nonlinear passive peaking EQ mode is modeled.

Physics-based methods are popular techniques in circuit modeling. They are more interpretable and flexible (since parametric) but efficiency in this case is not straightforward. Physics modeling can be computationally expensive since they are usually complex formulas and rely on the implicit scheme. In addition, the physics knowledge of the device and in particular the mathematical description may not be challenging to derive which can lead to introducing approximations in the simulated model.

Among data-driven block-oriented models, other popular approaches are the block-oriented Hammerstein model, the Wiener model, and their combinations [12]. In the Wiener model, a linear model is followed by a static nonlinearity, while in the Hammerstein model is the opposite. These models have a convenient representation, and they are created by estimating the model coefficients from real data and with some error minimization techniques. A proposed method to classify whether the nonlinear system should rather be modeled by a Wiener or a Hammerstein model is in [13]. Recent examples are for guitar distortion pedal [31] [32] [33], amplifier [34] [35], distortion circuit [36].

In the last two decades, ANNs have been extensively used for modeling analog audio devices. In particular, traditional ML techniques, initially developed for different purposes, have been investigated for creating models that emulate audio effects taking and processing raw audio samples, such as traditional DSP techniques.

In an early attempt using machine learning for audio effect modeling [37], a multilayer feedforward network was utilized to learn a high-pass filter and the Ibanez Tube-Screamer distortion effect. The author experimented with a network having one input layer, two hidden layers with sigmoid neurons, and one output layer with a linear activation function. The hidden and output layers present the same size as the input layer, and two different input sizes were considered in the experiments: 512 and 60 samples recorded at 44.1-kHz sampling rate. The training was performed using the MSE as loss function and feeding the network with overlapped segments, in particular, the hop size was half of the input size. The high-pass filter training was carried out on the frequency domain and led to unsatisfactory results, while the distortion effect was trained in the time domain and demonstrated the ability of the network to learn distortion effects. A spurious frequency was found to occur due to the overlapping process since the transition among frames was not sufficiently smooth. Feedforward networks are the simplest type of network, they do not incorporate mechanisms to learn time dependencies but their ability to encode the history of the signal only depends on the amount of input samples they take as input. This aspect limits their use to tasks not involving significant time dependencies.

Other attempts used convolutional-based networks to model the preamplifier circuit from the Fender Bassman 56F-A vacuum-tube amplifier [38]. The dataset has been built using a circuit simulator and the network consists of a stack of dilated causal convolution and fully connected layers. The first fully connected layer uses the gated activation function. The second layer has a hyperbolic tangent activation. Finally, a linear layer outputs the predicted sample. The error-to-signal ratio is the measure used as loss. The selected number of convolutional layers is 10 with a filter width of three and the dilation pattern  $d_k = 1, 2, 4, \dots, 512$ . This configuration leads to a receptive field of 2046 samples, corresponding to 46 ms of latency between the input and corresponding output sample, as it uses a sampling rate of 44.1-kHz. The model presents the fully connected layers with 8 and the convolutional layers with 16 units each. The number of samples used as input is set equal to the receptive field. The dataset was simulated with different values of the gain, which is a variable resistor, and used to condition the model. The conditioning is realized in the convolutional layers, and using the gated activation [39]. The work shows that CNNs accurately emulate the reference device better than a fully connected feedforward network and can respond to user control changes.

Using the same architecture, the Ibanez Tube Screamer, the Boss DS-1, and the Electro-Harmonix Big Muff Pi distortion pedals have been modeled as well [40]. The datasets in this case are collected directly from the devices. Here, the authors investigated more configurations: considering different dilation patterns, activation functions, such as rectified linear unit (ReLU), tanh, and gated activation, numbers of convolutional layers (10, 18, 24) and number of convolution channels (2, 4, 8, 16, and 32). In this work, the conditioning is not considered. A model with gated activation, 18 layers, and 16 convolution channels resulted in lower ESR and real-time capability.

Similarly to a fully connected feedforward network, convolutional networks' ability to track the past information in the signal depends on the receptive field, a longer

receptive field requires a greater number of layers. To overcome this problem, Temporal Convolutional networks (TCN) have been proposed for optical dynamic range compressors such as Teletronix LA-2A Leveling Amplifier [41], which present longer time-variant characteristics than distortion units. TCNs' strength consists of dilated convolutional networks with rapidly growing dilation factors ( $2^2$  and  $2^{10}$ ). Increasing the dilation factors increases in turn the receptive field and the ability of the networks when dealing with long dependencies while in turn not increasing the number of layers. In this case, the TCNs have been applied to 44.1 kHz sampled audio files. A TCN block consists of a convolutional layer, batch normalization, conditioning using FiLM, and PRelu activation function. Authors compared networks with 4, 5, and 10 TCN blocks, 32 convolutional channel for each convolutional layer, and 5, 13, 15 as the kernel size. The resulting models present receptive fields of 100, 300, and 1000 ms, respectively. The model with a receptive field of 300 ms provided the best performances. TCNs provide accurate and efficient implementation with respect to computational complexity. On the other hand, convolutional architectures present an intrinsic latency equal to the length of the receptive field, which is detrimental for live audio applications.

A model, that used a combination of different deep learning architectures, was investigated in [42]. In this case, the model is divided into three parts; an adaptive front-end, latent space, and synthesis back-end. The front-end performs time-domain convolutions with the raw audio to map it into a latent space. It also generates a residual connection which facilitates the reconstruction of the waveform by the back-end. The adaptive front-end consists of a convolutional encoder. It contains two CNN layers, one pooling layer, and one residual connection. The first layer has 128 filters and 64 channels and is followed by the absolute value as a nonlinear activation function. The second layer has 128 filters of size 128. The latent-space DNN contains two layers. The first layer is based on locally connected dense layers of 64 units and the second layer consists of a fully connected layer of 64 units. Both of these layers are followed by the softplus function. The DNN modifies the latent representation of the input audio into a new latent representation which is fed into the synthesis back-end. The synthesis back-end consists of an unpooling layer, a deep neural network with smooth adaptive activation functions (DNN-SAAF), and a single CNN layer. DNN-SAAF consists of four fully connected dense layers of 128, 64, 64, and 128 hidden units respectively. All dense layers are followed by the softplus function except the last layer. The SAAF [43] is used as the nonlinearity for the last layer. The model is first trained without the latent-space DNN and DNN-SAAF, and then these modules are incorporated for a second training. The loss function to be minimized is the mean absolute error (MAE). In both training procedures, the input and target audio are sliced into frames of 1024 samples with a hop size of 64 samples. Distortion, overdrive, and EQ effects have been modeled using this method, with a sampling rate equal to 16 kHz.

In [4] the previously described architecture is further explored and compared with different variations and with the CNN architecture based on [38]. The variations mainly consist of incorporating Bi-LSTMs or CNNs into the latent space. In this work, the target devices were Universal Audio Vacuum-Tube Preamplifier 610-B, Universal Audio Transistor-Based Limiter Amplifier 1176LN, and 145 Leslie Speaker

Cabinet. The highest score in the listening test was obtained by the variation incorporating Bi-LSTM. The input frame size was 4096 sampled with a hop size of 2048 samples. Another variation based on Bi-LSTM and SAAF as latent-space modules is used for plate and spring reverberators [44]. Here, the loss function to be minimized is the sum of MAE in the time domain and MSE of the log power magnitude spectra of the target and output. These architectures represent a general-purpose deep learning framework for modeling audio effects, which has been shown capable of accurately modeling different types of effects. On the other hand, the models are large networks with high computational complexity, leading to difficulty when considering efficient implementation. In addition, this architecture lacks conditioning possibility and focuses on modeling a static representation of the devices (i.e. fixed parameters).

The last group of machine-learning black-box modeling methods we review in this section are those based on RNNs. These have been applied to model a vacuum-tube amplifier [45], where authors investigated different networks and input sizes in two scenarios: slightly distorted and overdriven signals. The networks consisted of 5 or 10 units, while the networks' input included a variable number of audio samples. The network is autoregressive: it generates the output sample at the current time step using current and past input samples, but also output samples generated at previous time steps. The number of past samples can differ from the input and output signal, and in this case, the experiments considered 5, 10, or 50 input samples and 5 or 10 output samples. The work presents preliminary experiments and although the models resulted in poor performance, it demonstrates the feasibility of modeling vacuum-tube amplifiers with RNNs. Larger networks generated lower prediction errors and the overdrive case resulted in more challenges to model accurately.

RNNs, in particular LSTMs, have been also compared to CNNs when applied to the Ibanez Tube Screamer, the Boss DS-1, and the Electro-Harmonix Big Muff Pi distortion pedals [46]. The architecture consists of one RNN layer and one linear fully connected layer as an output layer with one unit. LSTM and GRU are compared as RNN layers varying the number of units (32, 64, and 96). The input signal is extended to include an additional value representing the user control's parameter. The results show that RNNs achieve similar accuracy to the CNN model, while requiring significantly less computational cost and latency, since requiring only the current input sample to predict the current output. LSTM performed better than GRU networks, and the error decreased when increasing the number of units. In addition, listening tests showed LSTM networks with 32 units performing similarly to TCN with 300 ms of latency [41].

Another RNN-based model utilized for the Klon Centaur guitar pedal circuit is presented in [47], which is also compared with a WDF model of the same circuit. ML implementation resulted in better computational performance than the WDF model but sounded very similar although the ML implementation has slightly damped high frequencies. The architecture consists of a GRU layer of 8 units and one linear fully connected layer with one unit as the output layer. Also here a single variable control parameter of the audio effect is added as an extra input, to condition the inference of the networks.



A delay-based effect is investigated in [48], where a tape-based delay is modeled using GRU networks using a 44.1kHz sample rate. Here, the delay trajectory is analyzed and extracted using impulse train signals. This trajectory is used to demodulate the signal before training the models or used to directly guide a delay-line built in a differentiable way and based on [1] work. The second strategy produced smaller prediction errors. The authors include the modeling of the tape’s noise and the trajectory using diffusion techniques to approximate the probabilistic distribution. The hidden size of the GRU layer was set to 64, and attempts with larger sizes led to no improvements.

RNNs rely on their internal memory mechanism to encode the history of the signal and system and allow the design of models to take a small number of input samples. In addition, they are compatible with real-time applications. On the other hand, they can still suffer from remembering significant long-term dependencies. Indeed, LSTMs alone have not been successful for LFO delay-based effects, such as flanger and phaser. In [49] authors found it beneficial to use as extra input the LFO signal representing the frequency response of a time-varying system over time. The LFO signal is first extracted by analyzing the recording at 44.1kHz and then used to help the LSTM during the learning process. The extra input has shown to be beneficial to learning the LFO-based effect and can be freely controlled after model training, although in the study is considered only static parameter values and not LFO signal changing depth and width over time. The error-to-signal ratio (ESR) is used as a loss function and the model is an LSTM layer followed by a linear fully connected layer with one unit. The size of the LSTM layer is 16 or 32 or 48.

A sequence-to-sequence-based model, based on LSTMs, was designed and proposed for the case of another optical compressor such as the TubeTech CL1B compressor [11], to help LSTMs’ memory. The network is based on two LSTM layers: one acts as an encoder the other as a decoder. The first takes a segment of past input samples together with the controls’ parameters, and the decoder takes the current input sample (in case of single output) or samples (in case of multi-sample output). The encoder, on processing the input, computes the internal states. These states are used as initial states for the second LSTM. These states represent a summary of the encoder input which helps the decoder to infer the output. The sequence-to-sequence-based model is compared to LSTMs and fully connected networks resulting in significantly better accuracy. The dataset, in this case, was at 48kHz sampling rate. The authors initially considered two control parameters: threshold and ratio, while attack and release parameters were fixed. In [50], the latter parameters were included. The encoder of the model was replaced with a convolutional layer and the model was compared to TCNs as well. Sequence-to-sequence-based models allow for more responsiveness and interactivity but at the expense of an increasing computational cost.

Other works consider hybrid approaches. In [3], fully connected neural networks exploit measurements within the circuits. Here, the structure includes 2 to 3 layers, embedded within a discrete-time state-space system and explored for diode-based guitar distortion circuits and the lowpass filter of the Korg MS-20 synthesizer. The method required measurements from the devices’ circuits, not always accessible, and is moving away from black-box models. Continuing towards gray box approaches, [51] is

based on the Differentiable Digital Signal Processing (DDSP) framework, and applies this concept to RC lowpass filter. Subsequently, the idea is applied to the parametric tone section of a guitar amplifier, and a nonlinear guitar overdrive circuit in [52]. The technique learns the parameters of a circuit model from measurements of real devices using a Wiener-Hammerstein model consisting of two IIR filters and a feedforward artificial neural network. The IIR filters are in this way trainable and derived from the analysis of the circuit. This approach is also used in [53]. In this case, a cascade of biquad filters is trained employing a Fourier transform, to model the BOSS MT-2 pedal distortion pedal. The model includes four tunable parameters. Differentiable Digital Filters have been applied for the case of a diode clipper circuit [54], showing higher accuracy and similar computation time when compared to traditional physics-based models. In [55], the authors proposed to learn ordinary differential equations governing the first-order and the second-order diode clipper using fully connected layers and RNNs. The formulation similarly uses the discrete-time state-space as in [3]. Neural networks have been also investigated in the case of wave digital filter formulations [2]. A tube amplifier circuit is simulated using multiport nonlinearities inside a wave digital filter and fully connected layers to learn features from a Kirchhoff-domain dataset. Similarly, in [56], authors combine recurrent neural networks (RNNs) with the Kirchhoff nodal analysis to create a grey-box guitar amplifier model. Lastly, an example of gray box modeling in the case of the LA-2A leveling amplifier is [57], where it is modeled starting from the structure of a traditional digital compressor but using fully connected and RNN to predict the compressor’s parameters.

Gray box methods have the advantage of helping the learning process with knowledge, potentially leading to more accurate and less computationally demanding models. On the other hand, internal measurement of circuit components is not always feasible because invasive or difficult to achieve. Infusing external knowledge could not be trivial. For example, in the case of an optical compressor, the attack and release time are governed by a lighting system whose behavior is difficult to model.

### 3 Methods

This study specifically investigates recurrent neural networks for virtual analog modeling. In particular, we aim to identify which type of recurrent layer or architectural configuration provides accurate modeling of different types of audio effects, if any. These architectures offer advantages due to their ability to capture time dependencies in the data by utilizing internal states, rather than solely relying on the input received at each iteration. In addition, we restrict the experimentation to relatively small networks, which present low computational complexity and low input-output, allowing implementation on real-time consumer-grade digital audio systems. We have developed models that exhibit minimal input-output delay and are well-suited for the typical audio processing workflow that operates on data in blocks. The designed architectures primarily consist of a recurrent layer along with a conditioning block. This architectural choice helps us incorporate control parameters. The designed models are applied to different audio effects and finally evaluated using different metrics. The primary objective of this study is to explore the capabilities of the different recurrent models in

learning from raw digital audio and effectively modeling audio effects. These insights can be used to understand the goodness and weakness of these models and which can suit better each audio effect. The models here presented, having limited parameters, are not expected to lead to perfectly accurate emulation, but a good starting point.

After selecting several types of analog audio effects to be included in this comparative study, as previously discussed, we have looked for existing public datasets including variable control parameters. In case these are not available, we recorded the dataset using analog effects within our availability. For those not available, we built the dataset using software plugins emulating specific analog effects. Datasets, for hardware or software effects, were collected using a tool that we have developed for this specific purpose <sup>1</sup>.

In the rest of this section, we first detail the four architectures used in this comparative study, then we present the the metrics we used for evaluating the trained models and the specific audio effects from which we collected the datasets. Finally, explain the process we used to train and test the models.

### 3.1 Architectures

The following architectures, based on different types of recurrent layers, are compared in this study: **LSTM** (a), **L-ED** (b), **LRU** (c), and **S4D** (d). The four architectures are illustrated in Figure 1. **L-ED** is based on the concept of internal state sharing [11]. All of these architectures follow the same design, consisting of recurrent layer, layer normalization, conditioning layer, and skip connections.

The number of input samples is identical for all architectures and set to 64. This choice represents a trade-off: on the one hand, there is the amount of past input information used to generate the current output, where more is typically better; on the other hand, there is the resulting input-output latency, which increases with the number of input samples. Our goal is to keep this latency below 1.33 ms (i.e., 64 samples at 48 kHz.). The input of all architectures is an array including the 64 most recent input sample, used to generate the single current output sample. As a consequence, the model is required to perform predictions at audio rate, one for each output audio sample. The models map a vector of 64 sample in one scalar output sample:

$$y_n = g(\mathbf{x}_n) = g(x_n, x_{n-1}, \dots, x_{n-62}, x_{n-63}) \quad (1)$$

where  $n$  is the discrete time index and  $g$  is the overall function describing the models. Before being fed into the recurrent layer (LSTM, LRU, or S4D), the input samples array  $\mathbf{x}_n$  is processed by a fully connected layer that performs a linear projection:

$$\mathbf{u}_n = \mathbf{W}_l \mathbf{x}_n + \mathbf{b}_l \quad (2)$$

where  $\mathbf{u}_n$  is the linear projected vector having a size equal to the number of hidden units of the fully connected layer.  $\mathbf{W}_l$  and is the weights' matrices, and  $\mathbf{b}_l$  the vector bias terms. The first two architectures use LSTMs as the recurrent layer, which was designed to improve the memory capacity of the vanilla RNN by incorporating

---

<sup>1</sup><https://github.com/stefanofasciani/DGMD>

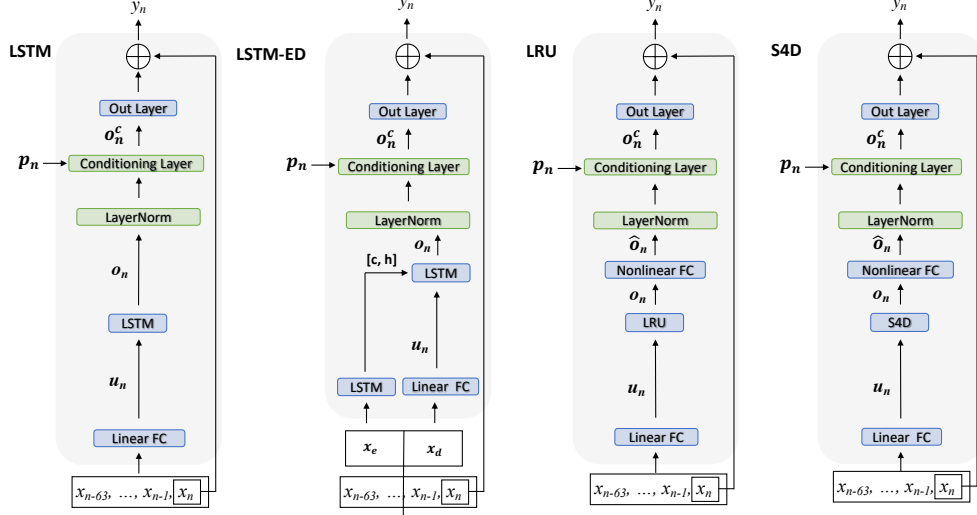


**Fig. 1** The four compared architectures: **LSTM**, **LSTM-ED**, **LRU**, and **S4D**. All architectures present the same structure: recurrent layer, layer normalization, conditioning layer, and skip connections. For the case of **LSTM-ED**, the input vector is equally split into two vectors,  $\mathbf{x}_e$  and  $\mathbf{x}_d$ . The first vector is used to feed an LSTM layer, which computes the internal states,  $[h, c]$ , that serve as initial states for a second LSTM layer, representing the actual recurrent layer. The input, identical in all four cases, is an array of the last 64 input samples  $[x_n, \dots, x_{n-63}]$ , which is used to produce the output sample  $y_n$ . The inputs are firstly linearly projected and then fed to the recurrent layer. Layer normalization is then performed before combining the conditioning information. Finally, the current output sample is generated through a skip connection, summing the output layer with the current input sample.

internal mechanisms known as gates, regulating the flow of information. The LSTM architecture is governed by the following equations:

$$\begin{aligned}
\mathbf{f}_n &= \gamma(\mathbf{W}_f \mathbf{h}_{n-1} + \mathbf{U}_f \mathbf{u}_n + \mathbf{b}_f) \\
\mathbf{i}_n &= \gamma(\mathbf{W}_i \mathbf{h}_{n-1} + \mathbf{U}_i \mathbf{u}_n + \mathbf{b}_i) \\
\mathbf{o}_n &= \gamma(\mathbf{W}_o \mathbf{h}_{n-1} + \mathbf{U}_o \mathbf{u}_n + \mathbf{b}_o) \\
\mathbf{c}'_n &= \phi(\mathbf{W}_c \mathbf{h}_{n-1} + \mathbf{U}_c \mathbf{u}_n + \mathbf{b}_c) \\
\mathbf{c}_n &= \mathbf{f}_n \circ \mathbf{c}_{n-1} + \mathbf{i}_n \circ \mathbf{c}'_n \\
\mathbf{h}_n &= \mathbf{o}_n \circ \phi(\mathbf{c}_n)
\end{aligned} \tag{3}$$

where  $\mathbf{h}_n$  is the hidden state vector,  $\mathbf{f}$  is the forget gate,  $\mathbf{i}$  the input gate, and  $\mathbf{o}$  the output gate, and  $\mathbf{c}$  is the cell state vector. The forget gate determines what information from previous steps should be kept or discarded. The input gate decides which information from the current step is relevant to add. The output gate determines the value of the next hidden state. Additionally, the cell state is updated by multiplying the forget vector and the input vector with new values that the neural network deems relevant. The forget vector and input vector are obtained using the sigmoid function,

denoted by  $\gamma$ , which determines how much information should be kept. Values of 0 in this vector indicate information to be discarded, while a value of 1 indicates information to be kept. Furthermore, the  $\phi$  represents the hyperbolic tangent function, used to keep the value of the cell state between  $-1$  and  $1$ . Finally,  $\mathbf{W}$  and  $\mathbf{U}$  are the weights' matrices, and  $\mathbf{b}$  the vector bias terms.

In the case of **LSTM-ED**, the input vector is equally split into two vectors,  $\mathbf{x}_d$  containing  $[x_n, \dots, x_{n-31}]$  and  $\mathbf{x}_e$  containing  $[x_{n-32}, \dots, x_{n-63}]$ . The first vector is fed to an LSTM layer, which computes the internal states,  $[\mathbf{h}, \mathbf{c}]$ , that serve as initial states for a second LSTM layer representing the actual recurrent layer. The second part of the input vector is linearly transformed and fed into the second LSTM, following the same procedure as the other models.

The third architecture is based on LRU. Compared to a vanilla RNN, the LRU uses a linear activation function used to compute the hidden state, instead of a nonlinear function. This modification allows the memory capability to improve significantly. The LRU equations are the following:

$$\begin{aligned} \mathbf{h}_n &= \mathbf{W}_h \mathbf{h}_{n-1} + \mathbf{U}_h \mathbf{u}_n + \mathbf{b}_h \\ \mathbf{o}_n &= \mathbf{W}_o \mathbf{h}_n + \mathbf{b}_o \end{aligned} \quad (4)$$

where  $\mathbf{h}_n$  is the hidden state at time  $n$  and acts as 'memory' of the network,  $\mathbf{o}_n$  the output vector. LRU keeps the recurrent layer linear but moves the nonlinearity to a subsequent fully connected layer. Additionally, to further enhance stability, the LRU incorporates a complex-valued diagonal recurrent matrix initialization, and an exponential parameterization, while a normalization scheme for the hidden states is used to boost the efficiency and accuracy [7].

Lastly, the SSMs operate by considering a continuous-time representation of the state-space formulation that is discretized to obtain the following equations:

$$\begin{aligned} \mathbf{h}_n &= \bar{\mathbf{W}}_A \mathbf{h}_{n-1} + \bar{\mathbf{W}}_B \mathbf{u}_n \\ \mathbf{o}_n &= \bar{\mathbf{W}}_C \mathbf{h}_n + \bar{\mathbf{W}}_D \mathbf{u}_n. \end{aligned} \quad (5)$$

The remarkable ability of SSMs to capture long-range dependencies stems from their utilization of a specific state matrix  $\bar{\mathbf{W}}_A$  known as the "HiPPO matrix" [58]. This matrix is designed to encode all the past input history in  $\mathbf{h}_n$ , finding a map from  $\mathbf{u}_n$  to a higher dimensional space  $\mathbf{h}_n$  that represents the compression of the history. The matrix allows the model to be conceptualized as a convolutional model that decomposes an input signal onto an orthogonal system of smooth basis functions. In this way, the state  $\mathbf{h}_n$  encodes the history of the signal. In our study, we employ the diagonal state space model variant, called S4D model [59], which is defined by parameterizing its state matrix as a diagonal matrix, boosting the efficiency of the model. By doing so, the basis kernels have closed-form formulas represented by normalized Legendre polynomials  $L_n(t)$ , resulting in the SSM decomposing the input signal  $\mathbf{u}_n$  onto an infinitely long set of basis functions that are orthogonal with respect to an exponentially decaying measure. This characteristic gives the SSM the ability to effectively model long-range dependencies.

The output size of the recurrent layer will be equal to the number of hidden units of the layer. In the case of LRU and S4D a fully connected layer with a softsign activation function also follows the recurrent layer, to compensate for a lack of nonlinear activation functions in these layers:

$$\hat{o}_n = \text{softsign}(\mathbf{W}_{nl}\mathbf{o}_n + \mathbf{b}_{nl}) \quad (6)$$

Subsequently, the Layer Normalization [60] is applied to help the training process. Layer Normalization estimates mean and variance which is then used to normalize the summed input to the weights, of the previously hidden layer on each training case. The mean  $\mu$  and the standard deviation  $\sigma$  are computed over all the weights of the previous layer to re-center and re-scale  $\mathbf{h}_n$ :

$$\hat{\mathbf{h}}_n = \frac{\mathbf{h}_n - \mu}{\sigma} \quad (7)$$

The conditioning block is then applied just before the output layer, which consists of a linear fully connected layer with one unit, which is described in the following subsection. Initial experiments indicate improved performance with the conditioning block is placed after the recurrent layers rather than before. This suggests that it is more beneficial for the networks to use the information given by the control parameters to project the output of the recurrent layer and determine the extent to which this information influences the final output, rather than influencing the inference of the recurrent layer based on the control parameters.

Finally, a skip connection is applied to the output of the output layer, which is a fully connected layer with one unit,  $y_n$ , where the input sample corresponding to the same time index  $n$  is added to  $y_n$ :

$$y_n = (\mathbf{W}_{out}\mathbf{o}_n^c + b_{out}) + x_n \quad (8)$$

where  $\mathbf{o}_n^c$  is the output of the conditioning block, as detailed in Figure 2. Since the output layer has one unit,  $\mathbf{W}_{out}$  is a vector of the same dimensionality as  $\mathbf{o}_n^c$ .

The number of units is chosen to have approximately 900 trainable parameters among the architectures and effects since an identical number is achievable due to major differences in the layers. As a result, the selected **LSTM** and **LSTM-ED** present 8 units in the recurrent layer and 4 in fully connected ones. **LRU** and **S4D** present 12 units in the recurrent layer, and 6 in fully connected ones. The number of trainable parameters also depends on the dimensional of the conditioning input  $\mathbf{p}$ , equal to the number of variable parameters in the datasets.

### 3.1.1 Conditioning Block

The conditioning block consists of the FiLM method and the GLU layer, as can be seen in Figure 2. FiLM is a technique that applies an affine transformation to a vector based on conditioning values. The parameters vector  $\mathbf{p}$ , if applicable, is the input to a linear fully connected layer. The output of this layer is then split into two vectors of equal size:  $\boldsymbol{\theta}$  and  $\boldsymbol{\eta}$ . If  $\mathbf{o}_n$  is the vector to which the transformation is to be applied, the

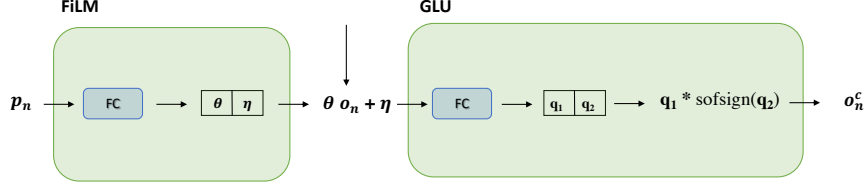


**Fig. 2** The Conditioning block operates as follows: the vector with conditioning values  $\mathbf{p}$  is first projected using a linear fully connected layer. This projection results in an output vector with twice the length  $\mathbf{p}$ . This output vector is then divided into two halves, labeled  $\boldsymbol{\theta}$  and  $\boldsymbol{\eta}$ . These vectors,  $\boldsymbol{\theta}$  and  $\boldsymbol{\eta}$ , are utilized to perform an affine transformation on the vector  $\mathbf{o}_n$ , coming from the recurrent layer. Subsequently, the transformed vector passes through another linear fully connected layer, producing another output vector that is double the length of its input. This output is also split into two halves, denoted as  $\mathbf{q}_1$  and  $\mathbf{q}_2$ . To complete the process, the softsign function is applied to  $\mathbf{q}_2$ , and the result is multiplied element-wise with  $\mathbf{q}_1$  to produce  $\mathbf{o}_n^c$ .

output of the linear fully connected layer will have a length double of  $\mathbf{o}_n$ . Consequently, FiLM performs an affine transform on  $\mathbf{o}_n$  using  $\boldsymbol{\theta}$  and  $\boldsymbol{\eta}$ .

Following the projection, it is common to apply a function, such as ReLU or sigmoid, to determine the amount of information that should be passed. In our approach, we replace the activation function with a GLU layer. This layer is more stable than ReLU and exhibits faster learning compared to sigmoid. Similarly to the previous step, the GLU layer consists of a linear fully connected layer that takes the FiLM output vector as input and computes a vector with twice its length. The resulting output is then split equally into two vectors:  $\mathbf{q}_1$  and  $\mathbf{q}_2$ . A function is applied to  $\mathbf{q}_2$ , and the resulting output is multiplied element-wise with  $\mathbf{q}_1$ . Hence, the conditioning block is described by the following:

$$\begin{aligned} \mathbf{o}_n^c &= \mathbf{q}_1 \otimes \text{softsign}(\mathbf{q}_2), \text{ with } \mathbf{q}_1 = \dot{\mathbf{o}}_n \mathbf{K}_1 + \mathbf{d}_1 \\ &\quad \mathbf{q}_2 = \dot{\mathbf{o}}_n \mathbf{K}_2 + \mathbf{d}_2 \\ \dot{\mathbf{o}}_n &= (\boldsymbol{\theta} \mathbf{o}_n + \boldsymbol{\eta}). \end{aligned} \quad (9)$$

The GLU layer determines the flow of information through the network, acting as a logical gate. Typically, a sigmoid activation function is used for this purpose. However, in our approach, we introduce a softsign function instead. The softsign function controls the extent to which the control parameters should positively or negatively influence the final output. A value of 0 indicates a bypass, meaning no influence on the output. This allows for more flexibility.

### 3.2 Losses and Metrics

The models in this study take raw audio samples as input and produce raw audio samples as output. The most common losses used in this case include the Mean Squared Error (MSE), the Mean Absolute Error (MAE), and the Error-to-Signal Ratio (ESR). Based on our knowledge and supported by empirical experiments, there is no evidence suggesting that more complex loss functions could benefit the learning process, especially when modeling the transformation applied to a signal by a generic audio effect.

While using specific and different loss functions for different effects may potentially yield better results, we decided to carry out this study using a fixed loss function across architectures and audio effects. This allows for a fair comparison between the trained models, as they all attempt to minimize the same loss function. Therefore, we selected the MSE for this comparative study as it helps to capture the dynamic aspects of the output signal more effectively [50].

In addition, our quantitative evaluation is based on various metrics to assess the models from different perspectives. In the following expressions,  $y_n$  and  $\hat{y}_n$  represent the target and predicted signal. The metrics compare  $y_n$  and  $\hat{y}_n$  using non-overlapping segments of the output signal with size  $W$  samples. The symbol  $N$  represents the overall number of samples in the output signal.

The first metric is the root-mean-square energy (RMSE) error, defined as:

$$M_{RMSE} = \frac{1}{N/W} \sum_{i=0}^{N/W} \left( \left| RMSE_i(y_n) - RMSE_i(\hat{y}_n) \right| \right), \quad (10)$$

$$\text{with } RMSE_i(y_n) = \sqrt{\frac{1}{W} \sum_{n=i*W}^{(i+1)W-1} |y_n|^2}$$

RMSE error provides insights into the energy deviation between the target and prediction. The RMSE envelope is calculated using a frame length  $W$  and hop size that is both equal to the minibatch size.

The losses and metrics presented so far, calculate the average difference between the target and prediction, which may hide large errors that occur only during signal transients. Transients, such as sharp attacks or decays, may represent a small fraction of the overall duration of an audio signal. In this case, we may obtain a relatively low error even with all transients poorly modeled. Therefore, we have included a metric that considers the differences between pairs of spectrums computed on consecutive overlapping windows, as used in the library <sup>2</sup> developed after [1]:

$$M_{SF} = \left\| \left( \left| |STFT(y_n)| - |STFT(y_{n-z})| \right| \right) - \left( \left| |STFT(\hat{y}_n)| - |STFT(\hat{y}_{n-z})| \right| \right) \right\|_1 \quad (11)$$

where the Short-Time Fourier Transform (STFT) is computed with a window size equal to 2048 and hop size equal to 512 samples. In the formula,  $z$  represents the hop size. This metric emphasizes the ability to accurately predict portions of the output sound with rapid changes.

---

<sup>2</sup><https://github.com/magenta/ddsp>



To account for the frequency response, we use the multi-resolution STFT [1]:

$$M_{STFT} = \frac{1}{N} \sum_m |||STFT_m(y_n) - STFT_m(\hat{y}_n)|||_1 + \frac{1}{N} \sum_m ||\log(|STFT_m(y_n)|) - \log(|STFT_m(\hat{y}_n)|)||_1 \quad (12)$$

which compares linear and logarithmic spectral distances with varying frequency resolutions using the L1 norm. The error is calculated as the sum of the absolute values of the vectors. This metric quantifies the error between the spectra employing different resolutions. We compute two separate multi-resolution STFT errors:  $M_{STFT-1}$  with FFT window lengths of  $m = [32, 64, 128]$ , and  $M_{STFT-2}$  with  $m = [256, 512, 1024]$ . This differentiation allows us to evaluate errors occurring in windows with high frequency but low time resolution separately from errors in windows with low frequency but high time resolution. For both cases, the hop size is 25% of the window length.

Similarly, we compare the MFCCs, to compute a metric linked to human sound perception:

$$M_{MFCC} = \frac{1}{N} |||MFCC(y_n) - MFCC(\hat{y}_n)|||_1 \quad (13)$$

where 1024 is the FFT length, and we have 80 Mel bands between 30 Hz and Nyquist frequency.

### 3.3 Audio Effects and Datasets

In this section, we introduce the audio effects selected for the study and the composition of their datasets. As already mentioned, in our search, we sought out publicly available datasets encompassing all the aforementioned types of analog audio effects and considering the presence of adjustable control parameters, if any. If we couldn't find these datasets online, we proceeded to record the dataset using effects that were at our disposal. In particular, we selected the following effects: overdrive, saturation, equalization, low-pass filter, and compression. Table 1 summarizes all the datasets included in the study. Delay-based effects require a different approach than a direct black box [49], [48]. For this reason, they are not included in this study.

The dataset we use is derived from the following hardware devices: Behringer OD300 overdrive pedal <sup>3</sup>, Behringer Neutron <sup>4</sup>'s overdrive module, Behringer Neutron's filter module in low-pass mode, TC Electronic Bucket Brigade Analog Delay used as a saturator <sup>5</sup>, CL 1B TubeTech <sup>6</sup> and Teletronix LA2A <sup>7</sup> optical compressors. We have also collected data from two software VA plugins: the Helper Saturator <sup>8</sup> and Universal Audio Pultec EQ <sup>9</sup>, because the hardware saturator presents no variable control parameter, and because we have no analog equalizer in our immediate availability.

---

<sup>3</sup><https://www.behringer.com/product.html?modelCode=P0608>

<sup>4</sup><https://www.behringer.com/product.html?modelCode=P0CM5>

<sup>5</sup><https://www.tcelectronic.com/product.html?modelCode=P0EBV>

<sup>6</sup><http://www.tube-tech.com/cl-1b-opto-compressor/>

<sup>7</sup><https://www.uaudio.com/hardware/la-2a.html>

<sup>8</sup><https://www.waproduct.com/plugins/view/helper-saturator>

<sup>9</sup><https://www.uaudio.com/uad-plugins/equalizers/pultec-passive-eq-collection.html>

### ***Overdrive***

Both the overdrive devices feature the following control parameters: volume, distortion level, and tone. The OD300 is a distortion pedal typically used with electric guitars, which features two different types of distortion, labeled overdrive and distortion modes. To record the dataset the unit was set to overdrive mode. The device was sampled at 5 different and equally spaced values for the distortion and tone knobs, between the minimum and maximum values, resulting in a 25 different combination. A separate output signal is recorded for each combination of the control parameters. Neutron’s Overdrive is a module integrated into the Neutron synthesizer. Thanks to the semi-modular nature of this device, we were able to isolate the overdrive module. We recorded the dataset’s varying distortion and tone as we did for the OD300, but sampling 10 equally spaced values for each parameter. In this case, we recorded the output for 100 different combinations of control parameters. In both devices, the volume level controls an attenuator, and we fixed this parameter to the maximum (i.e. no attenuation).

### ***Filter***

Similarly to the overdrive, the Behringer Neutron integrates a filter module, which features frequency cutoff and resonance knobs. The filter can be set as low-pass, high-pass, and band-pass. We isolated the module and recorded the dataset at 10 equally spaced values for the cutoff and 5 for the resonance. The cutoff parameter is between the minimum and maximum, while the resonance parameter is between the minimum to the mid value. having 100 different combinations and selecting the low-pass filter type. The filter was disconnected from the ADSR envelope module.

### ***Saturator***

Helper Saturator software emulates analog saturation, in particular tube and tape saturation. The software presents four parameters: lowpass and highpass cutoffs, saturation type switch (tape or tube), and saturation level. We recorded the dataset for 10 different values of the saturation level between minimum and maximum. The saturation switch was set to tape mode. Lowpass and highpass cutoffs were set to 20 and 20000 Hz, respectively.

The other device under this category is the TC Electronic Bucket Brigade Analog Delay pedal. The pedal is equipped with the well-known bucket brigade circuit, which consists of a series of capacitors that transmit the signal. By regulating the speed at which the capacitors fill and empty, a clock controls and slows down the signal, resulting in a delay as it passes through the bucket brigade device (BBD) circuit. The signal is sampled by storing an electric charge in a capacitor at each clock pulse. The sampling creates harmonic content and saturation. After traversing the BBD, the signal undergoes another low-pass filtering process, attenuating the new harmonics, and is expanded to match the dynamic range of the original input signal as closely as possible. Before entering the BBD section, the signal is typically manipulated as well, compressing and filtering using an anti-aliased filter.

This device features four knobs: time, feedback, volume, and depth, as well as a mode switch. The time knob determines the length of the delay, adjustable up to 600

ms. The feedback knob controls the number of repetitions of the delayed signal. The volume knob adjusts the volume of the delayed signal, while the depth knob defines the level of modulation. Activating the mode switch enables the modulation effect.

For our study, we primarily want to capture the processed signal without the delay component, which can be digitally simulated [61]. All knobs were set to their minimum values except for the volume knob, while the mode switch remained deactivated.

### *Equalizer*

The software plug-in Universal Audio Pultec Passive EQ emulates the tube-based equalizer Pultec EQP-1A. The effect presents low-frequency ([20, 30, 60, 100] Hz) and high-frequency ([3, 4, 5, 8, 10, 12, 16]kHz) switches to select the frequencies to boost or cut using the respective boost and attenuator knobs ([0,10]). Additionally, the emulation also has a bandwidth knob ([0,10]). The equalizer boosts and cuts the selected frequency bands, giving some saturation simultaneously. In this case, we recorded the dataset varying the boost and attenuator knobs at 5 different equally-spaced values up to half of their range, setting 60 Hz as the low-frequency switch value and 0 (sharp) as the bandwidth, obtaining 25 different recordings.

### *Compressor/Limiter*

The CL 1B and the LA2A are analog optical compressors. In optical compressors, a lighting-emitting element is fed with the audio signal that illuminates a light-sensitive resistor. The amplitude of the input signal determines the brightness of the element that, in turn, changes the resistance in the gain attenuation circuit. We used the available datasets [50] [62]. The CL 1B compressor dataset presents four parameters: attack, release, ratio, and threshold. To limit the data, we consider the threshold values range from 0 to 40 dBu, ratio values from 2:1 to 10:1, attack time from 0.5 to 300 ms and release time from 0.05 to 5 seconds. The total number of combinations was 375. In addition, we used the 25% of each recording. On the other hand, LA2A presents the peak reduction knob indicating the amount of compression ([0,100]) and a mode switch (limiter, compression), resulting in 200 combinations. Similarly to the CL1B dataset, we consider 25% of each recording.

### **3.3.1 Data Collection**

The data collection process was carried out using a MOTU M4 audio interface to feed a selection of audio signals into the system and simultaneously record its output. To achieve this, the left input channel of the audio interface was connected to the left output channel of the interface itself. The right input channel of the audio interface was connected to the output of the device, and the input of the device to the right output channel of the audio interface. This allows recording effectively both the device’s input and output signals compensating for the minor sound coloring and latency of the audio interface. The audio data was recorded at a sampling rate of 48 kHz.

The input mono signal differs if the device being measured includes control parameters or not. In particular, if any, the signal has a duration of 45 seconds for each parameter combination. If do not present any control parameter, to the signal is added other sound portions to achieve a duration of 20 minutes. The input signals include

**Table 1** Datasets with related parameters and ranges considered in the study.

	Type	Parameters	Range	Combinations
OD300 <sup>1</sup>	Overdrive	Level Tone	[min, max] [min, max]	25
Neutron’s OD module <sup>1</sup>	Overdrive	Level Tone	[min, max] [min, max]	100
Neutron’s Filter module <sup>1</sup>	Low pass filter	Cutoff Resonance	[min, max] [min, max]	100
BBD Analog Delay <sup>1</sup>	Saturator	-	-	n.a
Helper Saturator <sup>2</sup>	Saturator	Saturation Saturation Type	[min, max] Tape	10
Pultec Passive EQ <sup>2</sup>	Equalizer	Low frequency Frequency booster Bandwidth Frequency Attenuator	60 Hz [0,10] 0 [0,10]	25
LA2A <sup>1 3</sup>	Optical Compressor	Peak Reduction Switch Mode	[0,100] [Compressor,Limiter]	200
CL1B <sup>1</sup>	Optical Compressor	Threshold Ratio Attack Release	[-40, 0] dB 1:[1, 10] [5, 300] ms [0.005, 5] s	375

<sup>1</sup>Hardware.<sup>2</sup>Software.<sup>3</sup>Downloaded.

a variety of sounds, such as frequency sweeps covering a range of 20 Hz to 20 kHz, white noises with increasing amplitudes (both linear and logarithmic), recordings of instruments such as guitar, bass, drums (both loops and single notes), vocals, piano, pad sounds, and sections from various electronic and rock songs. Finally, the control parameter of each effect was mapped to the range of [0,1].

### 3.4 Experimenting and Learning

The models are trained for 60 epochs and using the Adam [63] optimizer with a gradient norm scaling of 1 [64]. The training was stopped earlier in case of no reduction of validation loss for 10 epochs. We design a time-based schedule for the learning rate as follows:

$$lr = \frac{LR}{e^4}, \text{ with } LR = 3 \cdot 10^4 \quad (14)$$

where LR is the initial learning rate, and  $e$  is the number of the epochs. Test losses and evaluation metrics are computed using the model’s weights that minimize the validation loss throughout the training epochs. Finally, the input signal is split into segments of 600 samples (equivalent to 12.5 ms), to be processed before updating the weights.

We adopted the same learning schedule and minibatch size for all models across all datasets. As explained in Section 3.3, we collected the datasets using the same approach and the same input file to minimize the difference among them. However, it is important to highlight that each dataset and modeling task may benefit from specific adjustments to achieve more accurate results. Different datasets and tasks may require slightly different learning rate schedules; an excessively slow or fast learning rate can lead to suboptimal solutions. The number of samples to process before updating the weights referred to as the minibatch size, impacts the frequency of updating weights: larger sizes may result in faster convergence but poorer generalization, while smaller sizes can aid generalization but may require additional epochs.

The composition of the training, validation, and test sets varies across datasets. For publicly available datasets such as LA2A, the three sets are already split and we utilized the sets in their original form. However, for the dataset we recorded, we used 80% for the training set, 10% for the validation set, and the remaining 10% for the test set. For effects with variable control parameters, each 45s recording in the dataset is associated with a specific combination of the effect parameters. The 80–10–10% split was carried out at the individual recording level, which ensures that all combinations of control parameters present an equal share in each subset, and are equally used for training and evaluation of the model. The initial 10% of all the recordings are used as the test set. The following 10% portion of the recordings is used as a validation set, while the remaining parts were used as the training set. Minor manual adjustments are made to ensure that splitting points fall within segments of silence.

## 4 Results

The evaluation is based on the metrics described in Section 3.2 and presented in Table 3, and 4. The MSE loss and the epoch-related epoch resulting in lower validation loss during training are reported in Table 2. The losses and the metrics consider all conditioning scenarios and provide an average error across all combinations of parameters. To further verify the model’s capacity to learn the conditioned effect, we provide a series of plots that compare the target signal with the predictions generated by the four distinct architectures. For these plots, we chose the modeling scenario that we believe to be the most challenging, based on the effect parameters used as conditioning factors for the networks. Except for the low-pass filter, this typically involves parameters at the maximum of the selected range since the output signal, under these conditions, is likely to deviate most significantly from the input. Regarding the low-pass filter, the parameters are configured for minimum cutoff and maximum resonance. The plots show the RMSE in Figure 3, the spectral flux in Figure 4, the spectra in Figure 5, and the spectrograms in Figure 6. For datasets including conditioning parameters, the plots showing predictions versus the target, are generated for a 2.5 seconds input signal containing bass, guitar, and drum loop sound. For the dataset without conditioning, the plots are generated from a 2.5 seconds input signal with percussive sounds. These input signals are part of the respective test sets. To ensure a clearer comparative visualization of the spectral flux, we use only the first 1.25 seconds.

In the OD300 overdrive dataset, the **LSTM** model presents the lowest MSE, MAE, and ESR, indicating better general amplitude matching between target and prediction. The **S4D** model is also accurate, especially when considering the transients and the RMS envelope. This can be observed from the lower error in terms of RMSE and spectral flux. On the other hand, in the case of maximum distortion, as seen in Figures 3 and 4, this superiority is less perceived. **LSTM-ED** and **LRU** are left behind except when looking  $M_{SF}$  where **LSTM-ED** show better performance than **LSTM**. Notably, the spectrograms shown in Figure 6 illustrate that **S4D** model generates more harmonics in the higher frequency region than **LSTM**, and especially than **LSTM-ED** and **LRU** whose produce a cleaner signal. This could be perceptually advantageous compared to the other model that poorly predicts such region of the spectrum, as summarized by the  $M_{MFCC}$  errors. From Figure 5 it is evident how the LSTM-based produces the best matching for energy at low frequencies. All models except **LRU** hit the early stop training condition at a relatively close epoch.

The Neutron OD dataset shows larger errors and it appears to be a more challenging modeling case for these architectures. Both **LSTM** and **S4D** models yield similar results in terms of average amplitude and frequency errors. **S4D** show slightly better performance. LSTM-ED surpasses the previous models in terms of RMSE, NESR, and SF, despite exhibiting a larger RMSE mismatch at maximum distortion settings, as visible in Figure 3. The spectrograms show less difference in harmonic distortion generation, as reflected in the frequency errors, which are very close to each other, although the **S4D** model exhibits lower errors. When informally listening, **S4D** tends to add more distortion than needed, while LSTM-based models do the opposite. Also in this case, **LRU** presents an early stopping epoch quite different than the other three cases.

For both the BBD and Saturator datasets, **S4D** outperforms all other models, while **LSTM-ED** is slightly less accurate. This is reflected also in the Figures 3 and 4. The **LSTM** and **LRU** models exhibit artifacts, as evident in Figure 6, which negatively impact performance, especially for **LRU**, and can be clearly heard when listening to the predicted output audio examples. The BBD dataset does not consider conditioning, unlike the saturator dataset, making it a simpler task, producing no significant deviation among the models' performances. The **LSTM** model tends to overpredict the energy at lower frequencies and underpredicts at higher frequencies, whereas the **LRU** model significantly underpredicts the signal amplitude compared to the other models. When informally listening, **S4D** model is the only one controlling the amount of saturation. The other models tend to overcharge the saturation.

In the case of the equalizer, LSTM-based models, specifically **LSTM** and **LSTM-ED**, exhibit slightly better performance compared to **LRU** and **S4D**. This holds also in the challenging conditioning scenario as visible in Figures 3, 4, 6, and 5.

The low-pass filter is relatively more difficult than the equalizer, as it introduces more drastic changes in the frequency contents of the processed signal. As the early stopping condition is met after a very few epochs, it appears that the model training converges quickly, as visible in Table 2. However, when informally listening to the predicted output, it is evident that all models fail in learning the filter behavior as they

simply attenuate the signal rather than removing high-frequency contents. Furthermore, the **LSTM** model produces better results when considering the time-domain metrics, but the errors are similar to other models when considering the frequency-domain ones. Also, the model tends to predict an excessive amount of energy in the lower portion of the spectrum, as visible in Figure 5. When considering the extreme conditioning case **S4D** performs better when considering RMSE, the transients, and spectrogram, as visible Figures 3 4 and 6.

**Table 2** MSE test loss computed on the test set. The test sets include all conditioning values, if applicable. The last column reports the epoch at which the training met the early stopping condition.

Dataset	Model	MSE	Epoch	Dataset	Model	MSE	Epoch
OD300	LSTM	$5.17 \cdot 10^{-4}$	60	Neutron's OD	LSTM	$2.87 \cdot 10^{-3}$	24
	L-ED	$8.06 \cdot 10^{-4}$	50		L-ED	$3.10 \cdot 10^{-3}$	60
	LRU	$7.91 \cdot 10^{-4}$	5		LRU	$3.31 \cdot 10^{-3}$	55
	S4D	$5.73 \cdot 10^{-4}$	52		S4D	$2.86 \cdot 10^{-3}$	60
Helper Saturator	LSTM	$4.53 \cdot 10^{-4}$	15	BBD Analog Delay	LSTM	$4.85 \cdot 10^{-6}$	59
	L-ED	$4.10 \cdot 10^{-4}$	60		L-ED	$5.14 \cdot 10^{-6}$	52
	LRU	$1.88 \cdot 10^{-3}$	60		LRU	$5.02 \cdot 10^{-6}$	36
	S4D	$3.99 \cdot 10^{-4}$	60		S4D	$4.49 \cdot 10^{-6}$	27
Pultec Passive EQ	LSTM	$1.29 \cdot 10^{-3}$	55	Neutron's Filter	LSTM	$3.13 \cdot 10^{-3}$	6
	L-ED	$1.35 \cdot 10^{-3}$	29		L-ED	$4.72 \cdot 10^{-3}$	3
	LRU	$1.69 \cdot 10^{-3}$	17		LRU	$4.10 \cdot 10^{-3}$	9
	S4D	$1.42 \cdot 10^{-3}$	18		S4D	$7.10 \cdot 10^{-3}$	1
LA2A	LSTM	$6.68 \cdot 10^{-4}$	14	CL1B	LSTM	$6.81 \cdot 10^{-4}$	28
	L-ED	$4.23 \cdot 10^{-4}$	21		L-ED	$6.69 \cdot 10^{-4}$	29
	LRU	$4.06 \cdot 10^{-4}$	55		LRU	$2.38 \cdot 10^{-3}$	30
	S4D	$3.73 \cdot 10^{-4}$	51		S4D	$6.66 \cdot 10^{-4}$	29

The optical compressor exhibits a time-variant response, and especially prolonged temporal dependencies dictated by the variable parameters of attack and release. This is particularly evident in the CL1B compressor, which poses a more challenging modeling task for neural networks. The **LSTM** model is the less accurate in this case. It presents a larger loss in both compressor cases. For the LA2A case, we can see a significant mismatch for RMSE and in transients phases, in Figure 3 and 4. In terms of the frequency domain, **S4D** provides a better match overall, although the **LSTM** model performs better in terms of MFCC error. Indeed spectrograms associated with LSTM-based models appear more similar to the target output than those associated with the **S4D** model. In the case of the compressor, the ability to encode past information is crucial, and **S4D** exhibits superior accuracy. The **L-ED** model is designed to improve the temporal tracking abilities of basic **LSTM**. This fact is confirmed by the results for both compressor devices. This improvement is particularly evident with the CL1B when setting long attack and release time through the conditioning control parameters. These reach up to 300 ms and 5 seconds, respectively. In Figure 3 and 4 difference across models is less marked, but the superiority of **S4D** is still clear. **LRU**

**Table 3** MAE, ESR,  $M_{RMSE}$ , and  $M_{SF}$  metrics computed on the test set. The test sets include all conditioning values, if applicable.

Dataset	Model	MAE	ESR	$M_{RMSE}$	$M_{SF}$
OD300	LSTM	$1.72 \cdot 10^{-2}$	$2.24 \cdot 10^{-1}$	$1.55 \cdot 10^{-2}$	$1.71 \cdot 10^{-2}$
	L-ED	$2.23 \cdot 10^{-2}$	$3.49 \cdot 10^{-1}$	$2.04 \cdot 10^{-2}$	$1.33 \cdot 10^{-2}$
	LRU	$2.29 \cdot 10^{-2}$	$3.42 \cdot 10^{-1}$	$2.18 \cdot 10^{-3}$	$2.48 \cdot 10^{-2}$
	S4D	$1.86 \cdot 10^{-2}$	$2.48 \cdot 10^{-1}$	<b><math>1.72 \cdot 10^{-3}</math></b>	<b><math>1.22 \cdot 10^{-2}</math></b>
Neutron's OD	LSTM	$2.68 \cdot 10^{-2}$	$3.16 \cdot 10^{-1}$	$2.44 \cdot 10^{-2}$	$8.06 \cdot 10^{-3}$
	L-ED	<b><math>2.56 \cdot 10^{-2}</math></b>	$3.41 \cdot 10^{-1}$	<b><math>2.31 \cdot 10^{-2}</math></b>	<b><math>5.10 \cdot 10^{-3}</math></b>
	LRU	$3.05 \cdot 10^{-2}$	$3.63 \cdot 10^{-1}$	$2.80 \cdot 10^{-2}$	$2.78 \cdot 10^{-2}$
	S4D	$2.69 \cdot 10^{-2}$	<b><math>3.15 \cdot 10^{-1}</math></b>	$2.42 \cdot 10^{-2}$	$6.48 \cdot 10^{-3}$
Helper Saturator	LSTM	$1.25 \cdot 10^{-2}$	$2.74 \cdot 10^{-1}$	$1.11 \cdot 10^{-2}$	$2.44 \cdot 10^{-2}$
	L-ED	$1.03 \cdot 10^{-2}$	$2.48 \cdot 10^{-1}$	$9.31 \cdot 10^{-3}$	$1.32 \cdot 10^{-2}$
	LRU	$2.77 \cdot 10^{-2}$	1.13	$2.00 \cdot 10^{-2}$	$3.90 \cdot 10^{-2}$
	S4D	<b><math>1.01 \cdot 10^{-2}</math></b>	<b><math>2.42 \cdot 10^{-1}</math></b>	<b><math>9.24 \cdot 10^{-3}</math></b>	<b><math>1.23 \cdot 10^{-2}</math></b>
BBD Analog Delay	LSTM	$1.33 \cdot 10^{-3}$	$1.69 \cdot 10^{-2}$	$1.28 \cdot 10^{-3}$	$1.56 \cdot 10^{-3}$
	L-ED	$1.36 \cdot 10^{-3}$	$1.79 \cdot 10^{-2}$	$1.31 \cdot 10^{-3}$	$1.35 \cdot 10^{-3}$
	LRU	$1.37 \cdot 10^{-3}$	$1.74 \cdot 10^{-2}$	$1.32 \cdot 10^{-3}$	$2.09 \cdot 10^{-2}$
	S4D	<b><math>1.29 \cdot 10^{-3}</math></b>	<b><math>1.56 \cdot 10^{-2}</math></b>	<b><math>1.24 \cdot 10^{-3}</math></b>	<b><math>8.13 \cdot 10^{-4}</math></b>
Pultec Passive EQ	LSTM	<b><math>1.61 \cdot 10^{-2}</math></b>	<b><math>3.75 \cdot 10^{-1}</math></b>	<b><math>1.40 \cdot 10^{-2}</math></b>	<b><math>2.09 \cdot 10^{-3}</math></b>
	L-ED	$1.66 \cdot 10^{-2}$	$3.92 \cdot 10^{-1}$	$1.44 \cdot 10^{-2}$	$2.98 \cdot 10^{-3}$
	LRU	$1.98 \cdot 10^{-2}$	$4.92 \cdot 10^{-1}$	$1.75 \cdot 10^{-2}$	$2.17 \cdot 10^{-2}$
	S4D	$1.77 \cdot 10^{-2}$	$4.14 \cdot 10^{-1}$	$1.56 \cdot 10^{-2}$	$4.76 \cdot 10^{-3}$
Neutron's Filter	LSTM	<b><math>2.45 \cdot 10^{-2}</math></b>	<b><math>8.16 \cdot 10^{-1}</math></b>	<b><math>1.84 \cdot 10^{-2}</math></b>	$3.03 \cdot 10^{-2}$
	L-ED	$2.91 \cdot 10^{-2}$	1.23	$2.23 \cdot 10^{-2}$	<b><math>2.16 \cdot 10^{-2}</math></b>
	LRU	$2.83 \cdot 10^{-2}$	1.06	$2.22 \cdot 10^{-2}$	0.11
	S4D	$3.85 \cdot 10^{-2}$	1.85	$2.14 \cdot 10^{-2}$	$2.31 \cdot 10^{-2}$
LA2A	LSTM	$1.65 \cdot 10^{-2}$	$2.22 \cdot 10^{-1}$	$1.57 \cdot 10^{-2}$	$5.48 \cdot 10^{-3}$
	L-ED	$1.48 \cdot 10^{-2}$	$1.50 \cdot 10^{-1}$	$1.44 \cdot 10^{-2}$	<b><math>4.53 \cdot 10^{-3}</math></b>
	LRU	$1.46 \cdot 10^{-2}$	$1.44 \cdot 10^{-1}$	$1.42 \cdot 10^{-2}$	$1.68 \cdot 10^{-2}$
	S4D	<b><math>1.36 \cdot 10^{-2}</math></b>	<b><math>1.32 \cdot 10^{-1}</math></b>	<b><math>1.33 \cdot 10^{-2}</math></b>	$6.54 \cdot 10^{-3}$
CL1B	LSTM	$1.39 \cdot 10^{-2}$	$5.78 \cdot 10^{-1}$	$1.16 \cdot 10^{-2}$	$9.36 \cdot 10^{-3}$
	L-ED	$1.26 \cdot 10^{-2}$	$5.69 \cdot 10^{-1}$	$1.02 \cdot 10^{-2}$	$9.04 \cdot 10^{-3}$
	LRU	$1.12 \cdot 10^{-2}$	2.07	$9.13 \cdot 10^{-3}$	$2.88 \cdot 10^{-2}$
	S4D	<b><math>9.54 \cdot 10^{-3}</math></b>	<b><math>5.67 \cdot 10^{-1}</math></b>	<b><math>7.49 \cdot 10^{-3}</math></b>	<b><math>8.27 \cdot 10^{-3}</math></b>

presents smaller errors than **LSTM** as well but it produces clearly audible artifacts, as visible in Figure 6.

Generally, for most effects considered in this study, performance metrics are fairly close across models. Although **S4D** outperforms other models by a small extent, considering the metrics only, it seems to be the most suitable architecture, among those included in this study, for generalizing the problem of analog effect modeling. **LSTM-ED** and in particular **S4D** are more efficiently encoding, inside the states, past signal information. Indeed in the case of optical compressors, they outperform other models



**Table 4**  $M_{STFT-1}$ ,  $M_{STFT-2}$ , and  $M_{MFCC}$  metrics computed on the test set. The test sets include all conditioning values, if applicable.

Dataset	Model	$M_{STFT-1}$	$M_{STFT-2}$	$M_{MFCC}$
OD300	LSTM	<b><math>5.06 \cdot 10^{-1}</math></b>	<b><math>4.25 \cdot 10^{-1}</math></b>	$6.56 \cdot 10^{-1}$
	L-ED	$6.82 \cdot 10^{-1}$	$6.44 \cdot 10^{-1}$	$7.85 \cdot 10^{-1}$
	LRU	$7.36 \cdot 10^{-1}$	$7.35 \cdot 10^{-1}$	$8.34 \cdot 10^{-1}$
	S4D	$5.99 \cdot 10^{-1}$	$5.88 \cdot 10^{-1}$	<b><math>6.13 \cdot 10^{-1}</math></b>
Neutron's OD	LSTM	$7.39 \cdot 10^{-1}$	$6.18 \cdot 10^{-1}$	$4.12 \cdot 10^{-1}$
	L-ED	$7.41 \cdot 10^{-1}$	$6.31 \cdot 10^{-1}$	<b><math>3.53 \cdot 10^{-1}</math></b>
	LRU	$7.90 \cdot 10^{-1}$	$6.81 \cdot 10^{-1}$	$5.01 \cdot 10^{-1}$
	S4D	<b><math>7.33 \cdot 10^{-1}</math></b>	<b><math>5.74 \cdot 10^{-1}</math></b>	$4.07 \cdot 10^{-1}$
Helper Saturator	LSTM	$5.50 \cdot 10^{-1}$	$5.27 \cdot 10^{-1}$	$5.48 \cdot 10^{-1}$
	L-ED	$5.41 \cdot 10^{-1}$	$5.01 \cdot 10^{-1}$	$4.59 \cdot 10^{-1}$
	LRU	1.19	1.53	0.533
	S4D	<b><math>5.29 \cdot 10^{-1}</math></b>	<b><math>4.95 \cdot 10^{-1}</math></b>	<b><math>3.90 \cdot 10^{-1}</math></b>
BBD Analog Delay	LSTM	$1.07 \cdot 10^{-1}$	$7.61 \cdot 10^{-2}$	$1.96 \cdot 10^{-1}$
	L-ED	$1.06 \cdot 10^{-1}$	$8.34 \cdot 10^{-2}$	<b><math>1.88 \cdot 10^{-1}</math></b>
	LRU	$1.09 \cdot 10^{-1}$	$7.49 \cdot 10^{-2}$	$2.65 \cdot 10^{-1}$
	S4D	<b><math>9.81 \cdot 10^{-2}</math></b>	<b><math>6.79 \cdot 10^{-2}</math></b>	$1.95 \cdot 10^{-1}$
Pultec Passive EQ	LSTM	<b><math>8.39 \cdot 10^{-1}</math></b>	<b><math>6.37 \cdot 10^{-1}</math></b>	$1.96 \cdot 10^{-1}$
	L-ED	$8.54 \cdot 10^{-1}$	$6.51 \cdot 10^{-1}$	$1.96 \cdot 10^{-1}$
	LRU	1.03	$8.96 \cdot 10^{-1}$	$2.98 \cdot 10^{-1}$
	S4D	$9.66 \cdot 10^{-1}$	$7.88 \cdot 10^{-1}$	<b><math>1.87 \cdot 10^{-1}</math></b>
Neutron's Filter	LSTM	<b><math>8.54 \cdot 10^{-1}</math></b>	<b><math>8.28 \cdot 10^{-1}</math></b>	$6.46 \cdot 10^{-1}$
	L-ED	$9.74 \cdot 10^{-1}$	$9.65 \cdot 10^{-1}$	<b><math>6.45 \cdot 10^{-1}</math></b>
	LRU	$9.80 \cdot 10^{-1}$	$9.75 \cdot 10^{-1}$	$7.57 \cdot 10^{-1}$
	S4D	$9.55 \cdot 10^{-1}$	$8.82 \cdot 10^{-1}$	$6.53 \cdot 10^{-1}$
LA2A	LSTM	$7.18 \cdot 10^{-1}$	$6.79 \cdot 10^{-1}$	<b><math>3.62 \cdot 10^{-1}</math></b>
	L-ED	$5.53 \cdot 10^{-1}$	$5.29 \cdot 10^{-1}$	$3.90 \cdot 10^{-1}$
	LRU	$5.40 \cdot 10^{-1}$	$5.11 \cdot 10^{-1}$	$4.28 \cdot 10^{-1}$
	S4D	<b><math>5.29 \cdot 10^{-1}</math></b>	<b><math>4.97 \cdot 10^{-1}</math></b>	$3.97 \cdot 10^{-1}$
Cl1B	LSTM	$8.97 \cdot 10^{-1}$	$8.61 \cdot 10^{-1}$	$3.20 \cdot 10^{-1}$
	L-ED	$6.57 \cdot 10^{-1}$	$5.62 \cdot 10^{-1}$	$3.17 \cdot 10^{-1}$
	LRU	$6.07 \cdot 10^{-1}$	$5.09 \cdot 10^{-1}$	$6.25 \cdot 10^{-1}$
	S4D	<b><math>4.34 \cdot 10^{-1}</math></b>	<b><math>3.23 \cdot 10^{-1}</math></b>	<b><math>2.87 \cdot 10^{-1}</math></b>

significantly. On the other hand, **LSTM** appears to perform well only when emulating effects where time-dependencies are shorter and less crucial, such as in the case of overdrive, equalizer, and filter. In addition, LSTMs tend to predict more accurately the energy on the low-frequency components. Finally, **LRU** seems to be not appropriate for modeling audio effects as they introduce major audible artifacts.

## 5 Conclusion

The computational challenges of simulating the nonlinearities of analog circuits, described by complex differential equations, are a significant obstacle for real-time

applications. The complexity of these nonlinearities makes them difficult to model accurately, but they also contribute to the unique sound characteristics of the devices, making them appealing for both academic and industrial purposes. Modeling these nonlinear aspects is a difficult task that requires simplifications and assumptions to ensure stability and efficiency in the numerical schemes. Artificial neural networks (ANN) have emerged as a popular data-driven approach for this modeling process. While they offer a convenient and automated approach, they may struggle with the computational complexity and flexibility required for handling control parameters. In some cases, hybrid solutions that incorporate physics knowledge or measurements from internal components may provide advantages. However, there are situations where black-box models are necessary and feasible. Recurrent neural networks (RNNs) utilize internal states as memory mechanisms, allowing them to encode the signal history. This feature enables more interactive solutions as their memory capacity is not solely dependent on the input amount. In this paper, we present a comparative analysis that examines the performance of the widely used Long Short-Term Memory (LSTM) models against recently proposed recurrent models, namely Linear Recurrent Unit (LRU) and State-Space models (SSM), which have demonstrated remarkable results in sequence modeling. To carry out this study, we design four models that incorporate parameter conditioning and emphasize low-latency response. The control parameters are integrated into the models using the Feature-wise Linear Modulation (FiLM) method. Our selection of effects includes overdrive, saturation, low pass filter, equalization, and compressors. We evaluate these models using various metrics, which provide valuable insights for future research and development. Specifically, our metrics consider the root-mean-squared energy envelopes, the transients, and the frequency content.

LSTM-based networks excel in replicating distortion and equalizer effects, showing their ability to effectively encode the audio dependencies enough for these specific effects. On the other hand, LSTM when designed in an encoder-decoder fashion, and in particular, SSMs outperform other models when emulating saturation and compression. In the case of compression, they demonstrate their advantage in accurately capturing the signal’s history. Conversely, LRUs produce less favorable outcomes, leading to noticeable audio artifacts. Generally, SSMs have proved to be an appropriate candidate technique also in VA, although the gap with the other models is not always so pronounced.

In this study, we did not carry out architecture- and effect-specific optimizations, which can definitely boost the accuracy, such as hyper-parameters tuning and changing the size of the various layers. We limited computational complexity and input-output latency and focused the study on models that can be theoretically implemented in consumer-grade devices for live audio applications.

In future work, conditioning techniques and performances should be further investigated. The current conditioning blocks rely on affine transformation, but devices such as distortion or saturation could benefit from more complex transformation to take into account the possible nonlinear influence of the parameters.

## References

- [1] Engel, J., Hantrakul, L., Gu, C., Roberts, A.: Ddsp: Differentiable digital signal processing. arXiv preprint arXiv:2001.04643 (2020)
- [2] Darabundit, C., Roosenburg, D., III, J.S.: Neural net tube models for wave digital filters. In: Proc. 25th Int. Conf. Digital Audio Effects (DAFx20in22), pp. 153–160 (2022). Vienna University of Music and Performing Arts Vienna
- [3] Parker, J., Esqueda, F., Bergner, A.: Modelling of nonlinear state-space systems using a deep neural network. In: Proceedings of the 23rd International Conference on Digital Audio Effects (DAFx-19), Birmingham, UK, pp. 2–6 (2019)
- [4] Ramírez, M., Benetos, E., Reiss, J.: Deep learning for black-box modeling of audio effects. *Applied Sciences* **10**(2), 638 (2020)
- [5] Hochreiter, S., Schmidhuber, J.: Long short-term memory. *Neural computation* **9**(8), 1735–1780 (1997)
- [6] Gu, A., Goel, K., Ré, C.: Efficiently modeling long sequences with structured state spaces. arXiv preprint arXiv:2111.00396 (2021)
- [7] Orvieto, A., Smith, S., Gu, A., Fernando, A., Gulcehre, C., Pascanu, R., De, S.: Resurrecting recurrent neural networks for long sequences. arXiv preprint arXiv:2303.06349 (2023)
- [8] Perez, E., Strub, F., Vries, H.D., Dumoulin, V., Courville, A.: Film: Visual reasoning with a general conditioning layer. In: Proceedings of the AAAI Conference on Artificial Intelligence, vol. 32 (2018)
- [9] Dauphin, Y., Fan, A., Auli, M., Grangier, D.: Language modeling with gated convolutional networks. In: International Conference on Machine Learning, pp. 933–941 (2017). PMLR
- [10] LeCun, Y., Bottou, L., Bengio, Y., Haffner, P.: Gradient-based learning applied to document recognition. *Proceedings of the IEEE* **86**(11), 2278–2324 (1998)
- [11] Simionato, R., Fasciani, S.: Deep learning conditioned modeling of optical compression. In: Proceedings of the International Conference on Digital Audio Effects (2022). DAFx Board
- [12] Schoukens, M., Tiels, K.: Identification of block-oriented nonlinear systems starting from linear approximations: A survey. *Automatica* **85**, 272–292 (2017)
- [13] Primavera, A., Gasparini, M., Cecchi, S., Hariya, W., Murai, S., Oishi, K., Piazza, F., Francesco: A novel measurement procedure for wiener/hammerstein classification of nonlinear audio systems. In: Audio Engineering Society Convention 144 (2018). Audio Engineering Society

- [14] Dieleman, S., , Schrauwen, B.: End-to-end learning for music audio. In: 2014 IEEE International Conference on Acoustics, Speech and Signal Processing (ICASSP), pp. 6964–6968 (2014). IEEE
- [15] Fettweis, A.: Wave digital filters: Theory and practice. *Proceedings of the IEEE* **74**(2), 270–327 (1986)
- [16] Paiva, D., R., *et al.*: *Circuit Modeling Studies Related to Guitars and Audio Processing*. Aalto University, ??? (2013)
- [17] D’Angelo, S.: *Virtual Analog Modeling of Nonlinear Musical Circuits*. Aalto University, ??? (2014)
- [18] Werner, K., Nangia, V., III, J.S., Abel, J.: Resolving wave digital filters with multiple/multiport nonlinearities. In: *Proc. 18th Conf. Digital Audio Effects*, pp. 387–394 (2015)
- [19] Kolonko, L., Velten, J., Kummert, A.: Automatic differentiating wave digital filters with multiple nonlinearities. In: *2020 28th European Signal Processing Conference (EUSIPCO)*, pp. 146–150 (2021). IEEE
- [20] Bernardini, A., Bozzo, E., Fontana, F., Sarti, A.: A wave digital newton-raphson method for virtual analog modeling of audio circuits with multiple one-port nonlinearities. *IEEE/ACM Transactions on Audio, Speech, and Language Processing* **29**, 2162–2173 (2021)
- [21] Dunkel, W., Rest, M., Werner, K., Olsen, M., III, J.S.: The fender bassman 5f6-a family of preamplifier circuits—a wave digital filter case study. In: *Proceedings of the International Conference on Digital Audio Effects (DAFx)*, Brno, Czech Republic, pp. 5–9 (2016)
- [22] Zhang, J., III, J.S.: Real-time wave digital simulation of cascaded vacuum tube amplifiers using modified blockwise method. In: *Proc. 21th Intl. Conf. Digital Audio Effects (DAFx-18)*,(Aveiro, Portugal) (2018)
- [23] Bogason, O., Werner, K.: Modeling circuits with operational transconductance amplifiers using wave digital filters. In: *Proc. 20th Int. Conf. Digital Audio Effects*, Edinburgh, UK, pp. 130–137 (2017)
- [24] Bogason, O.: *Modeling Auto Circuits Containing Typical Nonlinear Components with Wave Digital Filters*. McGill University, Canada (2018)
- [25] Bernardini, A., Werner, K., Maffezzoni, P., Sarti, A.: Wave digital modeling of the diode-based ring modulator. In: *Audio Engineering Society Convention 144* (2018). Audio Engineering Society
- [26] Chowdhury, J.: Real-time physical modelling for analog tape machines. In: *22nd*

- International Conference on Digital Audio Effects, Birmingham, UK, p. 3 (2019)
- [27] Werner, K., Abel, J.: Modal processor effects inspired by hammond tonewheel organs. *Applied Sciences* **6**(7), 185 (2016)
  - [28] Schaft, A.V.D., Jeltsema, D.: Port-hamiltonian systems theory: An introductory overview. *Foundations and Trends in Systems and Control* **1**(2-3), 173–378 (2014)
  - [29] Falaize, A., Hélie, T.: Passive guaranteed simulation of analog audio circuits: A port-hamiltonian approach. *Applied Sciences* **6**(10), 273 (2016)
  - [30] Najnudel, J., Remy, M., Hélie, T., Roze, D.: Identification of nonlinear circuits as port-hamiltonian systems. In: 24th International Conference on Digital Audio Effects (DAFx-21) (2021)
  - [31] Eichas, F., Möller, S., Zölzer, U.: Block-oriented modeling of distortion audio effects using iterative minimization. *Proc. Digital Audio Effects (DAFx-15)*, Trondheim, Norway (2015)
  - [32] Köper, L., Holters, M.: Taming the red llama—modeling a cmos-based overdrive circuit (2020)
  - [33] Darabundit, C., Wedelich, R., Little, F., NJ, P., Bischoff, P.: Digital grey box model of the uni-vibe effects pedal (2019)
  - [34] Jr, A.S., Bodmann, B.: Audio nonlinear modeling through hyperbolic tangent functionals. In: *Proceedings of the 19th International Conference on Digital Audio Effects (DAFx-16)*, pp. 103–108 (2016)
  - [35] Eichas, F., Möller, S., Zölzer, U.: Block-oriented gray box modeling of guitar amplifiers. In: *Proceedings of the International Conference on Digital Audio Effects (DAFx)*, Edinburgh, UK, pp. 5–9 (2017)
  - [36] Eichas, F., Zölzer, U.: Black-box modeling of distortion circuits with block-oriented models. In: *Proceedings of the International Conference on Digital Audio Effects (DAFx)*, Brno, Czech Republic, pp. 5–9 (2016)
  - [37] Mendoza, D.: *Emulating Electric Guitar Effects with Neural Networks*. Universitat Pompeu Fabra, Barcelona, Spain (2005)
  - [38] Damskögg, E.-P., Juvela, L., Thuillier, E., Välimäki, V.: Deep learning for tube amplifier emulation. In: *ICASSP 2019-2019 IEEE International Conference on Acoustics, Speech and Signal Processing (ICASSP)*, pp. 471–475 (2019). IEEE
  - [39] Oord, A., Dieleman, S., Zen, H., Heiga, Simonyan, K., Vinyals, O., Graves, A., Kalchbrenner, N., Senior, A., Kavukcuoglu, K.: Wavenet: A generative model for raw audio. *arXiv preprint arXiv:1609.03499* (2016)

- [40] Damskäg, E.-P., Juvela, L., Välimäki, V.: Real-time modeling of audio distortion circuits with deep learning. In: Proc. Int. Sound and Music Computing Conf.(SMC-19), Malaga, Spain, pp. 332–339 (2019)
- [41] Steinmetz, J., C., Reiss, D., J.: Efficient neural networks for real-time analog audio effect modeling. In: 152nd Audio Engineering Society Convention (2022)
- [42] Ramírez, M., JD, Reiss: Modeling nonlinear audio effects with end-to-end deep neural networks. In: ICASSP 2019-2019 IEEE International Conference on Acoustics, Speech and Signal Processing (ICASSP), pp. 171–175 (2019). IEEE
- [43] Hou, L., Samaras, D., Kurc, T., Gao, Y., Saltz, J.: Convnets with smooth adaptive activation functions for regression. In: Artificial Intelligence and Statistics, pp. 430–439 (2017). PMLR
- [44] Ramírez, M., Benetos, E., Emmanouil, Reiss, J.: Modeling plate and spring reverberation using a dsp-informed deep neural network. In: ICASSP 2020-2020 IEEE International Conference on Acoustics, Speech and Signal Processing (ICASSP), pp. 241–245 (2020). IEEE
- [45] Covert, J., Livingston, D.: A vacuum-tube guitar amplifier model using a recurrent neural network. In: 2013 Proceedings of IEEE Southeastcon, pp. 1–5 (2013). IEEE
- [46] Wright, A., Damskäg, A.E.-P., Välimäki, V., Vesa: Real-time black-box modelling with recurrent neural networks. In: 22nd International Conference on Digital Audio Effects (DAFx-19) (2019)
- [47] Chowdhury, J.: A comparison of virtual analog modelling techniques for desktop and embedded implementations. arXiv preprint arXiv:2009.02833 (2020)
- [48] Mikkonen, O., Wright, A., Moliner, E., Välimäki, V.: Neural modeling of magnetic tape recorders. arXiv preprint arXiv:2305.16862 (2023)
- [49] Wright, A., Välimäki, V.: Neural modeling of phaser and flanging effects. Journal of the Audio Engineering Society **69**(7/8), 517–529 (2021)
- [50] Simionato, R., Fasciani, S.: Fully conditioned and low-latency black-box modeling of analog compression. In: Proceedings of the International Conference on Digital Audio Effects (2023). DAFx Board
- [51] Kuznetsov, B., Parker, J., Esqueda, F.: Differentiable iir filters for machine learning applications. In: Proc. Int. Conf. Digital Audio Effects (eDAFx-20), pp. 297–303 (2020)
- [52] Esqueda, F., Kuznetsov, B., Parker, J.: Differentiable white-box virtual analog modeling (2021)

- [53] Nercessian, S., Sarroff, A., Werner, K.: Lightweight and interpretable neural modeling of an audio distortion effect using hyperconditioned differentiable biquads. In: ICASSP 2021-2021 IEEE International Conference on Acoustics, Speech and Signal Processing (ICASSP), pp. 890–894 (2021). IEEE
- [54] Chowdhury, J., Clarke, C.: Emulating diode circuits with differentiable wave digital filters (2022)
- [55] Wilczek, J., Wright, A., Välimäki, V., Habets, E.: Virtual analog modeling of distortion circuits using neural ordinary differential equations. Proc. Int. Conf. Digital Audio Effects (DAFx-22), Vienna, Austria (2022)
- [56] Miklanek, S., Wright, A., Välimäki, V., Schimmel, J.: Neural grey-box guitar amplifier modelling with limited data. In: International Conference on Digital Audio Effects, pp. 151–158 (2023). Aalborg University
- [57] Wright, A., Välimäki, V.: Grey-box modelling of dynamic range compression. Proc. Int. Conf. Digital Audio Effects (DAFx-22), Vienna, Austria (2022)
- [58] Gu, A., Albert, Dao, T., Ermon, S., Stefano, Rudra, A., Ré, C.: Hippo: Recurrent memory with optimal polynomial projections. *Advances in neural information processing systems* **33**, 1474–1487 (2020)
- [59] Gu, A., Goel, K., Gupta, A., Ré, C.: On the parameterization and initialization of diagonal state space models. *Advances in Neural Information Processing Systems* **35**, 35971–35983 (2022)
- [60] Ba, J., Kiros, J., Hinton, G.: Layer normalization. arXiv preprint arXiv:1607.06450 (2016)
- [61] Mačák, J.: Simulation of analog flanger effect using bbd circuit. In: Proceedings of the 19th International Conference on Digital Audio Effects (DAFx-16), Brno, Czech Republic, pp. 5–9 (2016)
- [62] Hawley, S., Colburn, B., Mimitakis, S.: Profiling audio compressors with deep neural networks. In: Audio Engineering Society Convention 147 (2019). Audio Engineering Society
- [63] Kingma, D., Ba, J.: Adam: A method for stochastic optimization. *Int. Conf. on Learning Representations* (2014)
- [64] Pascanu, R., Mikolov, T., Bengio, Y.: On the difficulty of training recurrent neural networks. In: International Conference on Machine Learning, pp. 1310–1318 (2013). Pmlr

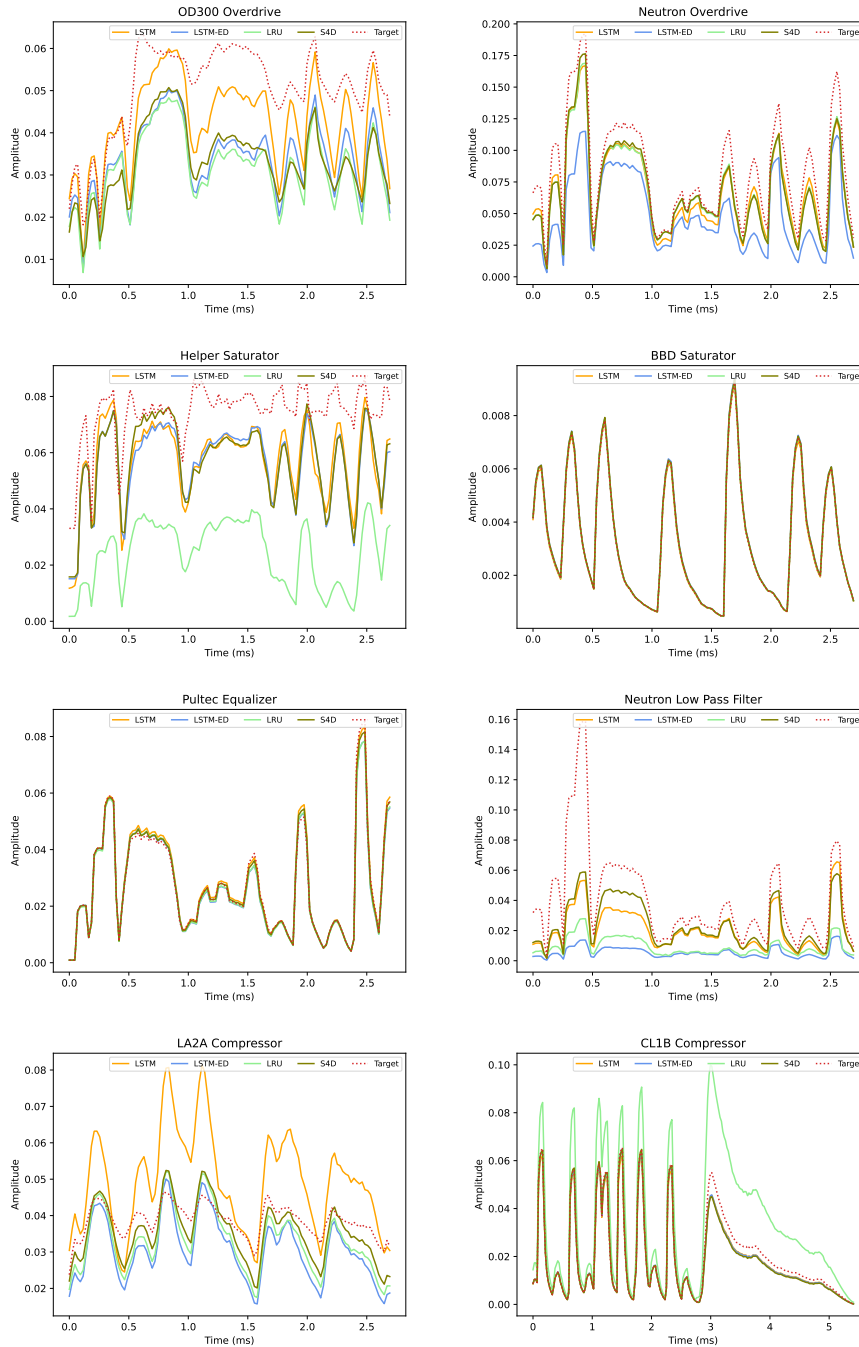


**Fig. 3** Comparison of the RMSE between the target and predicted output. The RMSE is computed using windows of 4096 samples with 75% overlap. When the model includes conditioning, the results refer to the highest conditioning values, representing the most challenging scenario.



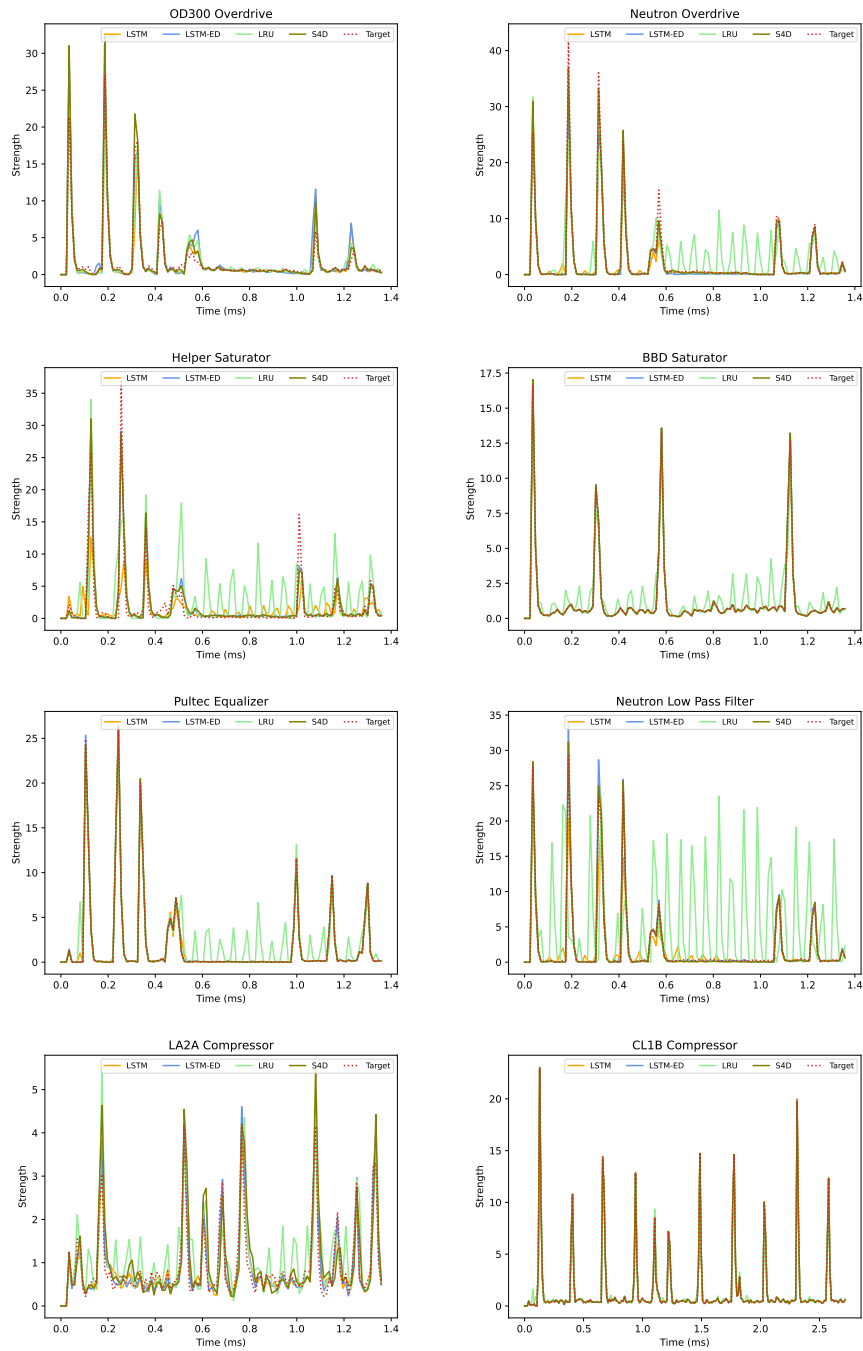


**Fig. 4** Comparison of the spectral flux between the target and predicted output. When the model includes conditioning, the results refer to the highest conditioning values, representing the most challenging scenario.

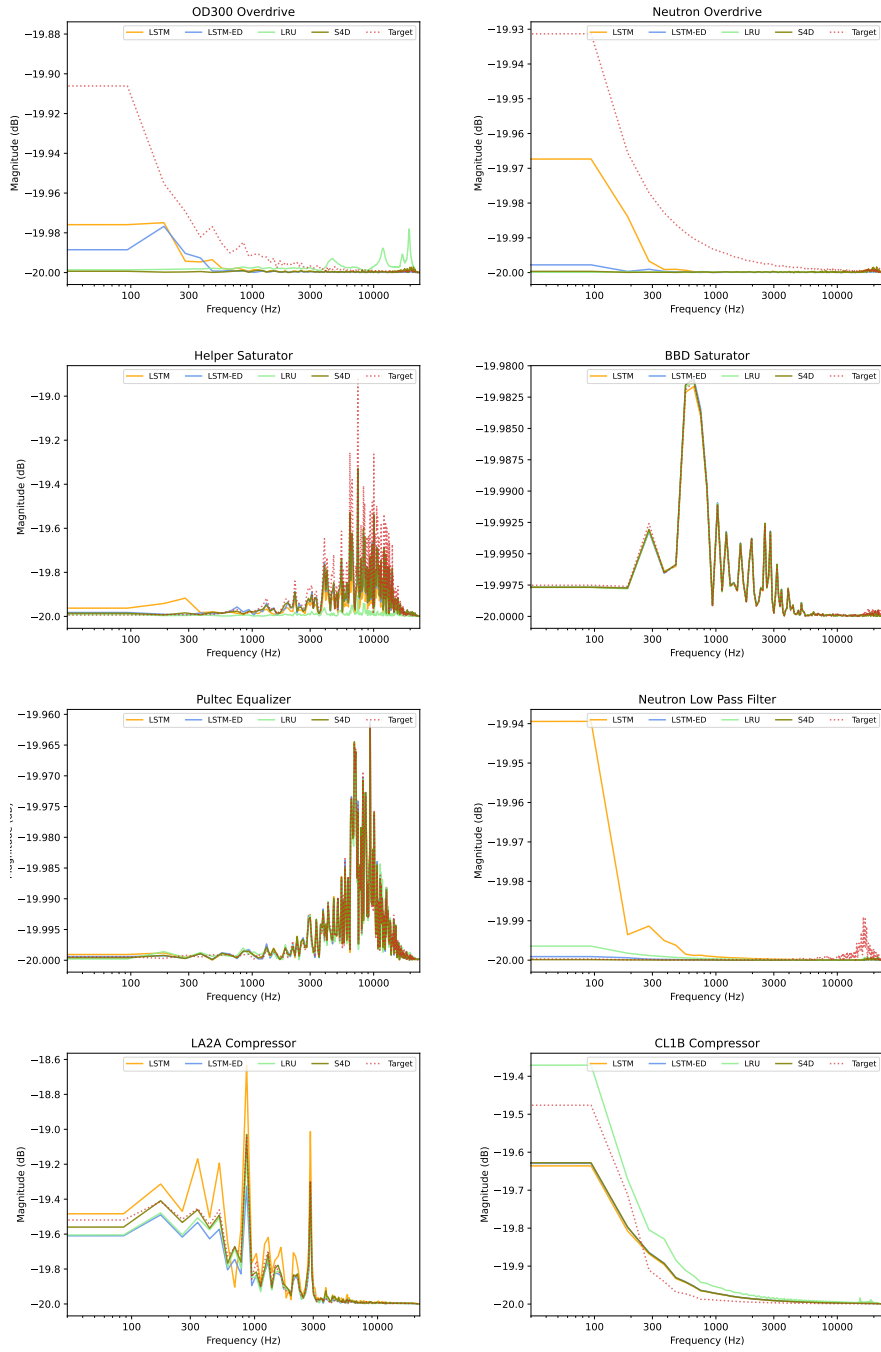


**Fig. 5** Comparison of the frequency content between the target and predicted output. The FFT is computed using windows of 512 samples. When the model includes conditioning, the results refer to the highest conditioning values, representing the most challenging scenario.

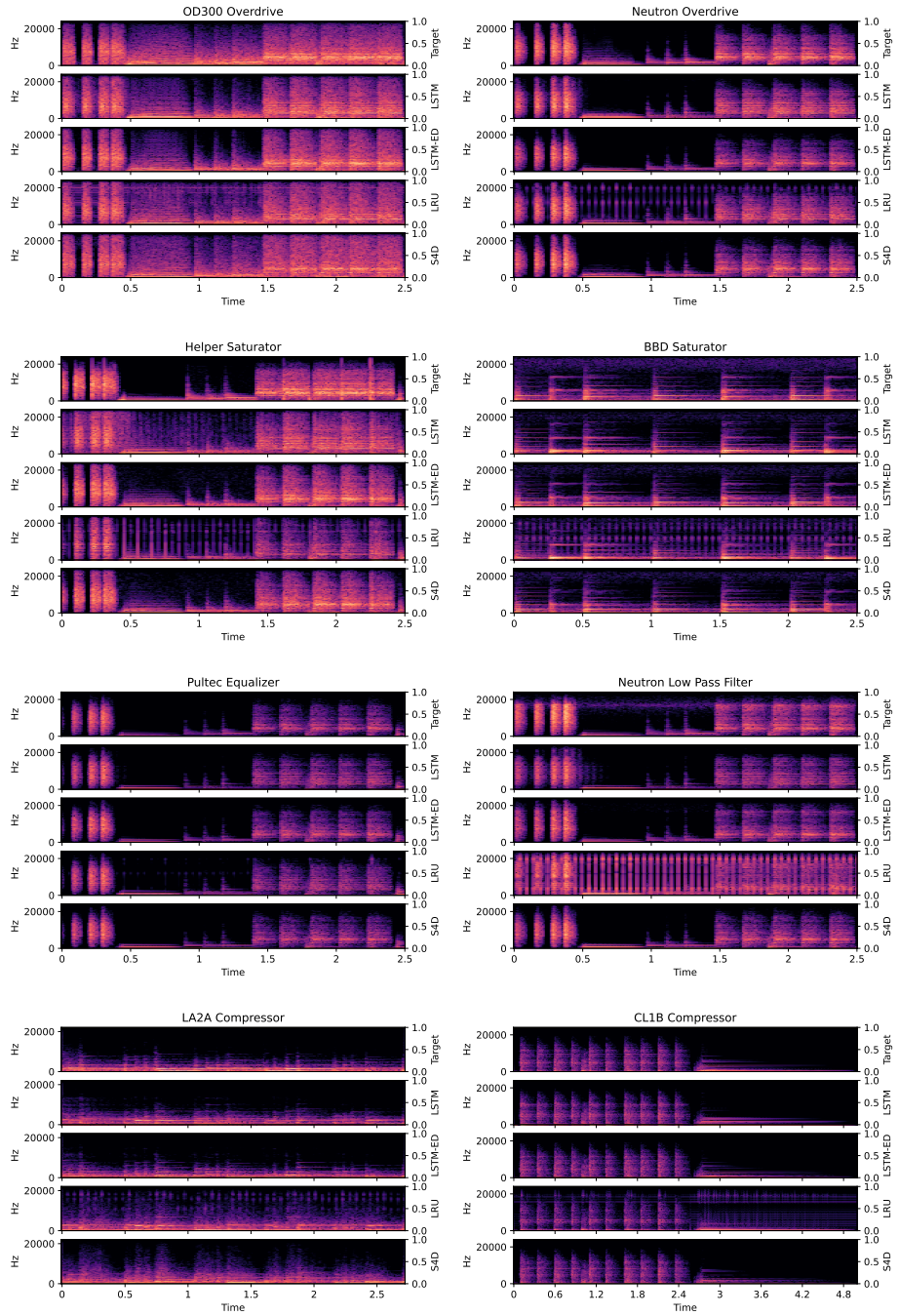


**Fig. 6** Comparison of spectrograms of the target and predicted output. The STFT is computed using windows of 2048 samples with 25% overlap. When the model includes conditioning, the results refer to the highest conditioning values, representing the most challenging scenario.